Journal of Geophysical Research Oceans
September 2008 ; Volume 113, C09014 : NIL_45-NIL_68
http://dx.doi.org/10.1029/2007JC004223

Transport and variability of the Antarctic Circumpolar Current south of Africa

Sebastiaan Swart[1, *], Sabrina Speich[2], Isabelle J. Ansorge[1], Gustavo J. Goni[3], Sergey Gladyshev[4], Johann R. E. Lutjeharms[1]

[1] Department of Oceanography, University of Cape Town, Rondebosch, 7701, South Africa.
[2] Laboratoire de Physique des Oceans, IFREMER, Universite de Bretange Occidentale, Brest, France.
[3] Atlantic Oceanographic and Marine Laboratory, Physical Oceanography Division, NOAA, Miami, Florida, USA.
[4] Shirshov Institute of Oceanology of the Russian Academy of Sciences, 36 Nakhimovskii Prospect, Moscow, 117997, Russia.

*: Corresponding author : Swart S., email address : sebastiaan.swart@uct.ac.za

Abstract:

Data from five CTD and 18 XBT sections are used to estimate the baroclinic transport (referenced to 2500 dbar) of the ACC south of Africa. Surface dynamic height is derived from XBT data by establishing an empirical relationship between vertically integrated temperature and surface dynamic height calculated from CTD data. This temperature-derived dynamic height data compare closely with dynamic heights calculated from CTD data (average RMS difference = 0.05 dyn m). A second empirical relationship between surface dynamic height and cumulative baroclinic transport is defined, allowing us to study a more extensive time series of baroclinic transport derived from upper ocean temperature sections. From 18 XBT transects of the ACC, the average baroclinic transport, relative to 2500 dbar, is estimated at 90 ± 2.4 Sv. This estimate is comparable to baroclinic transport values calculated from CTD data. We then extend the baroclinic transport time-series by applying an empirical relationship between dynamic height and cumulative baroclinic transport to weekly maps of absolute dynamic topography derived from satellite altimetry, between 14 October 1992 and 23 May 2007. The estimated mean baroclinic transport of the ACC, obtained this way, is 84.7 ± 3.0 Sv. These transports agree well with simultaneous in-situ estimates (RMS difference in net transport = 5.2 Sv). This suggests that sea level anomalies largely reflect baroclinic transport changes above 2500 dbar.

Keywords: Baroclinic transport; Antarctic Circumpolar Current; satellite altimetry.

3

1. Introduction

The Antarctic Circumpolar Current (ACC) flows, uninterrupted, around Antarctica. It is the primary means by which water, heat and salt are transported between the Atlantic, Indian and Pacific Oceans. These exchanges provide a vital mechanism for the global Meridional Overturning Circulation (MOC), which regulates the global climate system [Gordon, 1986; Rintoul, 1991; Sloyan and Rintoul, 2001; Rintoul, 2006; Speich et al., 2001; 2007a]. The spatial and temporal coverage of hydrographic measurements in the Southern Ocean remain severely limited by the logistic difficulty of sampling in this remote and harsh environment. This results in a poor understanding of the physical and dynamical processes that control the variability of the ACC and its influence on the MOC. The ACC is largely influenced by the oceanographic regimes that extend beyond its northern and southern borders. This is particularly true south of Africa where the ACC flows alongside the Agulhas Current system to the north. This system is regarded as one of the strongest western boundary currents in the world. Agulhas Rings, shed by the Agulhas Retroflection, are the primary means driving exchanges of water between the Indian and Atlantic Oceans [Byrne et al., 2006]. This leakage plays an important role on the MOC [Gordon, 1985; 1986; Weijer et al., 1999; Speich et al., 2007a]. The influence of the Agulhas Retroflection and associated ring shedding largely determines the latitudinal extent of the Subtropical Front south of Africa [Belkin and Gordon, 1996; G. Dencausse, pers. comm.], and, therefore, the northern limit of the ACC (Figure 1). South of the ACC, in this same sector of the Southern Ocean, the Weddell Gyre constitutes the largest cyclonic circulation regime in the Southern Ocean. The Weddell Gyre transfers heat and salt from the ACC to the Antarctic Continental shelves, where deep and bottom waters are formed [Orsi et al., 1993].

The GoodHope project launched in early 2004 [www.ifremer.fr/lpo/speich/GOODHOPE.htm; Ansorge et al., 2004; Speich et al., 2007a] aims to establish an intensive monitoring programme that will provide detailed information on the varying physical structure and volume flux of water masses and of the associated mass, heat and fresh-water fluxes between the Atlantic and Indian sector of the Southern Ocean. Sustained observations along the GoodHope cruise track provide the means to monitor the vertical thermal and salinity structure and variability of the ACC and its associated fronts. More extensive monitoring has been underway, since the 1970s, in Drake Passage [Sprintall et al., 1997], and in the Australian and the New Zealand 'chokepoints' [Rintoul et al., 1997; Budillon and Rintoul, 2003]. The deployment of XBTs by research and merchant vessels that supply the Antarctic bases provides an economical and rapid means to collect ocean temperature data. Nevertheless, these data need to be complimented by full depth CTD casts, current observations through Acoustic Doppler Current Profilers, current meter moorings or pressure

4

inverted echo sounder (PIES) arrays in order to robustly constrain the structure and variability of mass, heat and fresh-water transports through the widest 'chokepoint' of the Southern Ocean (approximately 4000 km between Africa and Antarctica). This vast distance and lack of scientific data in this remote region make the task of monitoring the Southern Ocean south of Africa very challenging.

A major objective of the GoodHope programme is to provide sound estimates of ACC transport and its variability. Previous ACC transport estimates in the region of the Greenwich Meridian came from Whitworth and Nowlin [1987] and Legeais et al. [2005]. Using CTD casts from the AJAX expedition, Whitworth and Nowlin [1987] estimated the baroclinic transport, relative to the bottom of the ACC, to be 162 Sv. From three CTD sections occupied near the Greenwich Meridian the baroclinic transports were averaged to 144.6 Sv, relative to the bottom, and 88.9 Sv, relative to 2500 dbar [Legeais et al., 2005]. Legeais et al. [2005], following Rintoul et al. [2002], used a proxy method based on an empirical relationship between upper ocean temperatures and the potential energy anomaly to derive the baroclinic transport of the ACC from 14 XBT sections near the Greenwich Meridian. The mean of these baroclinic transport estimates is 97.5 Sv, relative to 2500 dbar, and range from 87.5 Sv to 109.6 Sv.

In this study, we establish empirical relationships whereby dynamic height and baroclinic transport of the ACC can be determined from the upper ocean mean temperature alone. These relationships allow us to apply remotely sensed sea surface height (SSH) data to the proxy techniques, thereby enhancing the spatial and temporal sampling resolutions. One of the direct outcomes of this method allows us to monitor the upper ocean ACC thermal structure and its variability through the variability of the ACC fronts and SSH. These estimates are crucial in understanding the changes in the density field and its associated mass, heat and fresh-water transports. Our proxy methods prove to be robust by comparing our results to previous classical estimates and are very useful in an ocean region where observations remain scarce. Indeed, our understanding of how the ACC transport varies, even at seasonal scales, is still largely incomplete. As the ACC is the major component of the global ocean circulation, it is especially important to evaluate the internal variability of this large flow system and to identify interannual and long term changes in its transports, as they are intimately related to the interocean exchange of mass, heat and fresh-water. The combination of *in-situ* and remotely sensed data offers a powerful means to provide the first quantitative insight on the ACC transport variability.

The data used in this study are presented in Section 2. Section 3 describes the upper thermal structure and frontal variability between Africa and Antarctica primarily using XBT data. Detailed procedures and results, related to the proxy methods used to derive dynamic height data from the upper

5

ocean mean temperature alone, are explained in Section 4. In Section 5, we use the available hydrographic dynamic height data in the study region to derive baroclinic transport estimates of the ACC south of Africa and then analyse the meridional distribution of these transports in Section 6. In Section 7, transport estimates from satellite altimetry are discussed and compared to the CTD and XBT estimates. A time series of baroclinic transports, derived from satellite altimetry for the whole ACC and for each ACC front, is considered in Section 8. A summary completes the paper, where we go over the main points of the study and give some perspectives on further exploitation of the proxy methods we have presented here.

2. Data

2.1. Conductivity-Temperature-Depth

We use data from six CTD sections completed in the South-East Atlantic between November 1983 and October 2005. The sections provide a good coverage of the seasonal variability expected in the South-East Atlantic region because they are occupied during all seasons (Table 1). While the first four of these data sets come from historical observations (from 1984 to 1993), the last two of them consist of the first two repeats of the GoodHope transect completed by the Shirshov Institute of Oceanology, aboard the RV Akademik Sergey Vavilov [Gladyshev et al., 2007]. The two CTD occupations along the GoodHope line allow us to improve the accuracy of the baroclinic transport estimates from those already made by Legeais et al. [2005]. This is because the two GoodHope cruises are occupied over the same cruise track (in different years) and the water column was sampled with a relatively high spatial resolution (each station is separated by approximately 45 km). In total, we use data from 276 CTD casts (of which 232 stations lie within the ACC domain), which connect Cape Town to Antarctica primarily following a ground track of the satellite altimeters (track no. 133 of Topex-Poseidon initially, followed by Jason1) till the Greenwich Meridian from where the GoodHope transect continues south to the Antarctic continent (Figure 2). The AJAX and A21 transects have the coarsest spatial resolution, where stations are spaced approximately 100 km apart as opposed to a 75 and 88 km spacing between stations occupied by the A12 and SR2-WOCE sections, respectively. The first GoodHope CTD section has a mean spacing of 43 km, while the mean station spacing for the second GoodHope CTD section is 56 km. In most cases, tighter station spacing is found over regions of dynamic or steep bottom topography. The closer spacing between the GoodHope CTD casts allow us to include ‘snapshots’ of the mesoscale structure of the flow along the whole GoodHope transect (the characteristic length scale of eddies and meanders is greater than 100 km in diameter). Details concerning the CTD calibration, station positions, bottle analysis, problems encountered,

6

and sampling carried out on each cruise can be found in a series of technical reports and papers [SIO, 1985; Roether et al., 1990; Lemke, 1992; Gladyshev et al., 2007].

2.2. Expendable Bathythermograph (XBT)

The XBT data, in part, originates from 13 sections completed close to the Greenwich Meridian (Figure 3), between 1989 and 2006, as part of German and Russian research cruises and one ferry service completed by the University of Cape Town. Apart from the August 1989 transect, sampling took place during summer months, between November and March. In addition to this, five repeat high-density XBT sections have been completed since February 2004 along the GoodHope cruise track, as part of the GoodHope and the AOML Atlantic high-density XBT programs. The ocean structure is extremely well resolved by using XBTs deployed at high resolution. This proves to be particularly important when studying the dynamics and variability of the ACC as its flow is composed of discrete and intense narrow jet-like structures [Sokolov and Rintoul, 2007a; 2007b].

During the GoodHope transects, XBTs were deployed to measure the upper ocean temperature at intervals of 25 km, increasing the frequency to 15 km over the frontal regions of the ACC. Most deployments reached a maximum working depth of the Sippican Deep Blue XBT, which is in the order of 780 m. The GoodHope and Alfred Wegner Institute (AWI) XBT transects are sampled with a vertical resolution of 2 dbar, while the section completed by the Arctic and Antarctic Russian Institute (AARI) has a vertical resolution of 1 dbar. The 4000 km transect between Africa and Antarctica was on average completed within two weeks, with each section providing a roughly synoptic picture of the upper thermal layer in this sector of the Southern Ocean.

Extensive quality control procedures have been applied to the XBT data by AOML/NOAA in the United States. Adjacent temperature profiles were compared with each other and to the Levitus climatology [Levitus, 1982] in the region. Profiles were declared bad and discarded if they did not reach a minimum depth of 400 dbar. When feasible and if the temperature data recovered well, 'spikes' in the profile were removed and edited. For more details on AOML quality control procedures, refer to Bailey et al. [1994] and Daneshzadeh et al. [1994].

2.3. Satellite altimetry data

2.3.1. Sea level anomaly

7

Satellite altimetry measurements of SSH are used to estimate baroclinic transport. The 'Maps of Sea Level Anomaly (MSLA)' product from CLS/AVISO, a weekly SSH anomaly map on a 1/3° Mercator grid that incorporates T/P, Jason-1, ERS-1/2 and Envisat altimeters, was used in this study. Because the ACC is characterized by fine scale structures and variability we choose to use the "up to date" data processing that makes use of all the satellite data available for each period. The satellite data, for this time series, are not homogeneous in number but for long periods they provide an improved resolution and data accuracy compared with the classical "referenced" data set. These multi-mission gridded SSHs are referenced to a seven year (1993-1999) mean. For details on mapping methods and error corrections applied to these fields, refer to Le Traon et al. [1998], Le Traon and Ogor [1998] and Ducet et al. [2000].

2.3.2. Absolute dynamic topography

The 'Maps of Absolute Dynamic Topography (MADT)' product from CLS/AVISO has the same temporal and spatial resolution described in the sea level anomaly section. The MADT is the sum of the sea level anomaly data and a mean dynamic topography [Rio05 – Combined Mean Dynamic Topography (CMDT); Rio and Hernandez, 2004]. The CMDT is a combined product using *in-situ* measurements (hydrographic and surface drifter data), altimetry data and the EIGEN-GRACE 03S geoid. The CMDT is computed over a seven year period (1993-1999).

3. Upper ocean thermal structure and frontal variability south of Africa

South of Africa, the ACC flows between the South Atlantic and South Indian subtropical domains in the north and the eastern part of the Weddell Gyre in the south. The criteria and classical position of the following fronts observed in this region: the Subtropical Front (STF), the Subantarctic Front (SAF), the Antarctic Polar Front (APF), the southern ACC front (sACCf) and the southern boundary of the ACC (SBdy) are listed in Table 2. A time sequence of six XBT sections (five repeat GoodHope occupations and an Antarctica - Cape Town section) between 2004 and 2006 (Figure 4), depicts the temporal and latitudinal variability of the upper ocean temperature structure in the Atlantic sector south of Africa.

Significant thermal variability is produced in the form of mesoscale structures: eddies, meanders and narrow, intense horizontal temperature gradients corresponding to the jet-like structure of the ACC [e.g., Sokolov and Rintoul, 2007a]. An almost continual presence of eddies are found in the northern domain of the GoodHope section (located between 34-39°S). These features are spawned at the Agulhas Current Retroflection, where large Agulhas Rings detach from the Agulhas Current and spin into the

8

Atlantic Ocean [Duncombe Rae, 1991; Lutjeharms, 1996; de Ruiter et al., 1999]. SSH and RAFOS float data illustrate this region as a ‘cauldron’ of turbulent mesoscale activity, which may directly influence the stability and continuity of the STF south of Africa [Belkin and Gordon, 1996; Boebel et al., 2003]. For this reason we question the use of the STF as a northern delimiter of the ACC in Section 7.

A weekly time series of the MADT data shows that Agulhas Rings propagate towards the south-west and cross the GoodHope transect, between 39-42°S, on approximately 1-2 occasions per year. Agulhas rings further complicate the process of defining the STF because they transfer subtropical water signatures into the ACC realm. Furthermore their anticyclonic rotation result in large transport reversals in the ACC [Richardson, 2007; Gladyshev et al., 2007; refer also to Section 6]. We identify these features using MADT data and back-track their trajectories to confirm their point of origin is within the Agulhas Current Retroflection (Figure 5). The centre of an Agulhas Ring is marked by a black circle on Figure 5. During October, 19, 2005, the feature can be seen propagating, in a west-southwest direction. By December, 7, 2005, the western limit of the feature has crossed the GoodHope transect (dashed line), at approximately 40.5°S. The fifth GoodHope XBT transect (Figure 4e) crosses the same feature on December, 5, 2005. Only the western edge of the ring is encountered. As a result of the ring being only clipped during the December 2005 transect, the thermal signal of the XBT data appears to be less dominant than the January 2005 transect, which bisected a larger proportion of a ring at ~42°S (Figure 4c). In addition, an Agulhas Ring is located in the Subantarctic Zone (SAZ), in the December 2005 section (Figure 4e). The temperature sections, where these features are located, reveal a warming of the waters to ~700 m, with surface temperatures ranging from 19.0°C (January 2005) to 15.5°C during the December 2005 occupation. The Agulhas Ring, seen in January 2005 causes a strong subsurface meridional temperature gradient between <8°C to >13°C over a distance of <60 km. The diameter of the warm core eddy, defined by the maximum horizontal temperature gradient ($\Delta T/\Delta x$) at 200 m, is approximately 170 km. Even though this constitutes a strong warm anomaly, for this region, it does not seem to affect the latitude of the SAF at 44.22°S, but rather it strengthens the temperature gradient across the front. In contrast, due to the absence of warm or cold mesoscale features in the remaining sections, the horizontal temperature gradient, between 41-44°S, decreased at a steady rate, without large temperature fluctuations.

9

The latitude of the ACC fronts for the six XBT transects[1] are shown in Figure 6 (during three of the GoodHope transects the SBdy was not reached so we do not include it in our present discussion). The XBT-inferred positions of the ACC fronts are generally found slightly south of the traces by Orsi et al. [1995]. The only discrepancy comes from the path of the SAF, where Orsi et al. [1995] show the front to steer south (~47.6°S) of Meteor Rise, located at approximately 47°S, 7°E. The XBT and CTD sections, described in this study, which cross Meteor Rise, show that the SAF is, on all occasions, located to the north of this rise in bathymetry.

The sequence of frontal latitudes (Figure 6) reveals a southward shift in both the SAF and APF, at least during the spring and summer months. Between 2004 - 2006, the SAF moved 1.16° (130 km) southward while the APF shifted 2.65° (294 km). For the last three sections (between October 2005 and February 2006) some of the southward signal could be induced by seasonal warming of the upper thermal layer between spring and the late summer months. This is suggested by the temperature anomaly sections for each of the XBT realizations (Figure 7). The three sections, between October 2005 and February 2006, shows that the temperature anomaly, in the upper 150-200 m layer, adjusts from <-1°C to >1°C. Taking the latitudes of the SAF and APF for two February months (2004 and 2006), a southward movement in these two fronts is evident and corresponds to a warmer upper ocean state. The comparison is only made over two years, so it is likely that this large southward shift in the fronts is part of the short-term variability experienced in the region. In order to understand how much of this southward movement forms part of long-term southward trend, we will need a greater ensemble of data. Nonetheless, it is important to note that Gille [2002] has analysed temperature data from Lagrangian floating platforms to show that the Southern Ocean, and in particular the ACC, has warmed by 0.17°C since the 1950s. A possible explanation is the 50 km southward shift in the ACC. More recently, Cai [2006] has shown a trend in the positive wind stress curl (1978 and onward from NCEP/NCAR reanalysis), induced by Antarctic ozone depletion. This trend drives an intensifying, southward shifting of the Southern Ocean super-gyre circulation [Speich et al. 2002; 2007b]. It is suggested that the trend in winds and related ocean circulation leads to a greater influx of warm water to the south in all three oceans, and contributes to an increased rate of warming in the polar region. This may explain the southward shift in the ACC fronts as observed over a short period here, and over a longer period, as observed by Gille [2002].

[1] The February 2006 section does not follow the GoodHope cruise track and, therefore, some spatial differences occur. However, variability in the altimeter SSH field is small (<3 cm) for the latitudinal bands of the SAF and APF (between February 2004-2006). This reveals that no significant change in the XBT-derived frontal positions results from the distance between the two sections.

4. Dynamic heights from XBT data

Rintoul et al. [1997] have shown that a tight correlation exists between the average upper ocean temperature and dynamic height south of Australia. Furthermore, Rintoul et al. [2002] suggest that across the ACC the T-S curve is stable enough to estimate dynamic heights using temperature data alone. In the present study we show that this correlation exists also in the ACC region south of Africa (r = 0.95, significant at the 95% level). This relationship proves to be extremely useful because XBT data, which is limited to only the upper 800 m, can be used to derive dynamic heights at the surface. To test this relationship, several average temperatures within pressure ranges were assessed (e.g. 100-200 dbar, 300-400 dbar, 100-600 dbar, 600-700 dbar and 0-600 dbar). The strongest correlation exists when utilizing the average temperature between 0-600 dbar and the dynamic height at the surface (relative to 2500 dbar). Moreover, the 0-600 dbar level was best suited to maximise the data available, instead of extending the level to 700 or 800 dbar. Figure 8 shows the empirical relationship between the temperature averaged between 0-600 dbar and the dynamic height at the sea surface, relative to 2500 dbar, using data from the six CTD sections completed in the Atlantic sector south of Africa (see Figure 2). Four of these CTD sections were used because they were sampled in adjacent areas of the GoodHope transect, while the remaining two CTD sections were occupied along the GoodHope transect. The fact that the sections are not sampled in precisely the same location has no significant impact on deriving dynamic height using these proxy methods. This is because the upper ocean average temperature is a proxy for a streamline of the ACC and we assume that conservation in the streamline will occur to some extent upstream and downstream of the GoodHope transect.

Although the CTD sections were occupied in different seasons, the data collapse onto a single curve, confirming that this relationship is stable for this region of the Southern Ocean. The shape of the curve, between approximately 4-7°C, generally reflects the meridional variation of temperature from ~46°S to 42°S. The drop in dynamic height below 4°C results in a steep dynamic height gradient, which is caused primarily by the southward increase in upper ocean salinity (34.3 to 34.7 psu) and fall in meridional ocean temperature between 46°S and 55°S. The larger scatter of points, where temperatures exceed 7°C, is due to the influence of Agulhas Water introduced by Agulhas Rings north of the STF. The mean dynamic height decline across the ACC for the six CTD sections is 1.1 ± 0.06 dyn m (1 dyn m = 10 m^2s^{-2}). The northern and southern boundaries of the ACC are taken as the position of the STF and southern boundary (SBdy), respectively [from Orsi et al., 1995].

We plot the average ocean temperature, between 0-600 dbar ($T_{0\text{–}600}$), from the 18 available XBT sections, to investigate their latitudinal dependence (Figure 9). The data points fall on a relatively tight curve over the ACC, but diverge at the northern and southern ends. North of the ACC domain (~ 40°S), the presence of a highly energetic field of anticyclonic and cyclonic eddies largely originating from the Agulhas Retroflection area (as already mentioned in Section 3), allows for a zonal and meridional exchange of Atlantic, Indian and Southern Ocean water masses. The upper ocean thermal structure in this region is thereby variable, causing the upper ocean temperature range to spread significantly. The SBdy marks the frontier separating waters flowing in the ACC from those found in the cyclonic sub polar Weddell Gyre. Poleward of the SBdy, the gradient in dynamic height tends to zero. Two XBT sections ($IX3_1$ and $IX3_2$) cross the Maud Rise, located at 65°S, 3°E. The upper ocean average temperatures are higher than sections located further away from the Maud Rise (see Figure 9). Gordon and Huber [1995] note that a quasi-stationary pool of relatively warm Weddell Deep Water (WDW) appears immediately west of the Maud Rise. This feature is derived from the flow of warm WDW around the flanks of Maud Rise. The rise in upper ocean temperature identified in the XBT data, over the Maud Rise, has a direct influence on overestimating the dynamic height data later on. This overestimate however does not have any bearing on the dynamic heights estimated over the ACC.

In order to estimate dynamic height from the available XBT sections, we exploit the empirical correlation, shown in Figure 8, by applying a smoothing spline to the data. Fifth and eighth order polynomial fits were also tested and applied to the data. However, the smoothing spline provides a better method for the approximation of values for this dataset. In recent years, it has been generally accepted [Emery and Thomson, 2001] that the smoothing spline is the most effective approximation method.

To assess the ability of this method to infer dynamic height from XBT temperature data, we first compare the actual dynamic height, relative to 2500 dbar, to the estimates predicted by the regression relationship for the six available CTD transects. In order to avoid bias, we withhold each of the six CTD section's dynamic height values from the empirical relationship, before predicting the dynamic height using the temperature observations. The results and corresponding root mean square difference (RMSD) over the ACC domain are shown in Figure 10. The mean of the RMSD for the six CTD sections is 0.05 dyn m. The agreement between the two estimates is excellent and the RMSDs are small. Discrepancies between the two estimates are largest near the northern and southern boundaries of the ACC, where the empirical relationship is less tight. This is likely due to the mixing of different water masses found at the boundaries and where the spread of upper ocean temperature increases (as shown in Figure 9). Due to the higher spatial resolution of the two CTD sections (~50 km), occupied along the GoodHope cruise track, mesoscale features are better resolved, causing the dynamic height data to vary more than found in the remaining four CTD sections, that have lower spatial resolutions. The ACC fronts, especially the SAF and APF are well represented in the dynamic height gradients.

Dynamic heights are now estimated from the 18 XBT sections using the empirical relationship. These estimates have a marked latitudinal dependence, particularly within the ACC domain, and compare closely with true dynamic heights from the CTD sections (Figure 11). Once again, the values north of the STF exhibit a large dispersion due to the large temperature range in the upper ocean associated with this region. For the purpose of this study, we focus specifically on the ACC, i.e. on the domain between the STF and the currents southern boundary, where the empirical relationship is particularly stable.

We illustrate the dynamic height estimates for the five GoodHope repeat XBT transects in Figure 12. The mean net dynamic height drop from the northern to the southern boundary of the ACC for the five XBT sections is 1.1 ± 0.065 dyn m, which is the same as the mean CTD dynamic height drop off. The range of the dynamic height drop across the ACC is between 1.01 dyn m in February 2004 to 1.20 dyn m in November 2004. This indicates a range of 0.19 dyn m variability over the ACC. The three inner frontal (SAF, APF and sACCf) positions are marked along the dynamic height profiles. Local maxima in the dynamic height gradient can be seen over the SAF, during the GH2 (November 2004) and GH3 (January 2005) transects. The dynamic height drop across the APF and sACCf is well reproduced during all the transects. The rise and fall in the dynamic height, between the STF and SAF, is mostly induced by the presence of mesoscale eddies (i.e. Agulhas Rings) that were crossed during the first and third GoodHope transects. In addition to the maximum gradient in the dynamic height over the identified 'classical' fronts, we see further drops in the dynamic height. These are mostly associated with the APF and suggest that the 'classical' ACC fronts could be associated with additional baroclinic jets as suggested by Sokolov and Rintoul [2007a] south of Australia. The identification of these additional jets is explained, in more detail, in Section 7.

The evidence shown here indicates that we can determine the Southern Ocean frontal positions where large gradients in dynamic heights are encountered. This suggests the position of the fronts can be determined from gradients of satellite SSH.

5. Baroclinic transports from XBT data

In order to derive baroclinic transports of the ACC from temperature data alone, we derive a second empirical relationship between dynamic height, relative to 2500 dbar (DH_{2500}), and cumulative baroclinic transport, integrated northward and above the 2500 dbar isobath (CT_{2500}) (Figure 13). This relationship is constructed using data from five of the CTD transects completed in the South-East Atlantic. We did not make use of the baroclinic transport data from the SR2 section, since a large proportion of the stations did not reach 2500 dbar. This method has been used to derive baroclinic transports from altimeter data for the region south of Australia [Rintoul et al., 2002]. Similarly to Rintoul et al. [2002], we use 2500 dbar as the reference level because it is the deepest depth that lies above the height of the mid-ocean ridge. The correlation between the two variables is very tight ($r = 0.98$, significant at the 95% level), meaning we can estimate baroclinic transports using dynamic height data. Again a smoothing spline is applied to the data.

We evaluate the accuracy of inferring baroclinic transports from upper ocean temperature data. The empirically derived dynamic heights for the CTD sections were first computed using upper ocean temperature data by exploiting the $T_{0\text{–}600}$–DH_{2500} relationship and then applying it to the DH_{2500}–CT_{2500} relationship to derive baroclinic transports. These transports were then compared to baroclinic transport estimates derived from the five CTD sections, relative to 2500 dbar. Resulting baroclinic transports and RMSDs are shown in Figure 14. The mean RMSD for the five tested sections is 6.0 Sv (1 Sv = 10^6 m^3s^{-1}). This RMS error between baroclinic transports is relatively high however the total end transports, cumulated from south to north, compare well. The mean baroclinic transport for the five sections is 87.9 ± 3.9 Sv compared with DH_{2500}–CT_{2500} derived baroclinic transports, which averaged 91.5 ± 1.2 Sv. On average, cumulative baroclinic transport values obtained from the DH_{2500}–CT_{2500} relationship exceed CTD derived baroclinic transports by 3.5 Sv, or only 4% higher.

We apply this proxy method to 18 XBT sections located in close proximity to the CTD transects. Several XBT sections are situated further eastward of the CTD transects. These sections exhibit a poleward shift in the STF in this region causing the average northern ACC limit on the XBT lines to be displaced southward relative to the average value from the CTD transects (41.8°S versus 40.3°S) [Legeais et al., 2005]. The XBT-inferred ACC baroclinic transports (above and relative to 2500 dbar; Tr_{2500}) range from 85.2 Sv to 94.7 Sv, with a mean of 90.0 ± 2.4 Sv. This is only 2.1 Sv (or 2.3%) higher than the 87.9 ± 3.9 Sv average from the CTD sections. Figure 15, shows the baroclinic transport for the five repeat GoodHope sections and the Antarctica-Cape Town (AA-CT) section between February 2004 and February 2006. Differences in baroclinic transport, at each station pair, are represented by the stems. Large increases in net baroclinic transport occur over the main fronts of the ACC. The substantial increase and then decline in baroclinic transport near the northern end of the GH3 section is as a result of the intense Agulhas Ring that was crossed. These baroclinic transport estimates are biased towards the summer months when sampling primarily occurred.

There is no clear inter-annual pattern in net baroclinic transport. The net baroclinic transport does, however, tend to increase during the mid to late summer months when compared to sections completed in the early summer/spring months of the same season. The temperature sections show that the isotherm gradients steepen as the seasonal progression warms the upper ocean layers. This increases the horizontal gradient in the dynamic height, which in turn intensifies the eastward baroclinic flow. The temperature at the southern end of the section is relatively constant with time, and, therefore, an increase in baroclinic transport tends to correspond to the presence of higher temperatures (and temperature gradients) in the northern domain of the ACC.

The mean XBT baroclinic transport estimate, made here, is 7.5 Sv lower than that measured by Legeais et al. [2005]. Our empirical relationships are constructed, partially, using the South-East Atlantic historic CTD sections used by Legeais et al. [2005] however we include two additional recent repeat CTD sections conducted along the GoodHope cruise track. The historic CTD sections are occupied at a lower spatial resolution and are not located along the GoodHope cruise track, which may, in part, be the cause of the final transport disparity. The GoodHope CTD sections do display net baroclinic transport estimates that are ~4 Sv less than the historic CTD estimates. Additionally, thermal changes in the upper ocean layers, incurred during the temporal gap (9-18 years) between the recent and the historic CTD occupations, may lead to the transport differences between the two studies.

The average of the bottom referenced transport for four CTD sections is 145.0 ± 9.4 Sv. Due to the fact that CTD casts did not reach the bottom in the majority of the stations comprising the second CTD occupation of the GoodHope cruise track, no baroclinic transports relative to the bottom could be obtained for this section. The ratio between the baroclinic transport above 2500 dbar and to the bottom is almost constant and averages approximately 0.62 ± 0.055. This ratio proves to be a useful parameter to estimate the full depth baroclinic transports (Tr_{bottom}) from XBT-inferred transports at 2500 dbar. When applying the 62% Tr_{2500}/Tr_{bottom} ratio, the bottom XBT-inferred ACC baroclinic transport ranges between 139 and 153 Sv, with a mean of 145 ± 3.9 Sv, for the 18 XBT crossings. These estimates agree with those obtained by Legeais et al. [2005], who use the I6 CTD section conducted along 30°E, in addition to the three historic CTD sections conducted in the South-East Atlantic, to derive bottom referenced transports form XBT data.

This ratio has also been observed in other regions of the ACC. Along the SR1 transect in Drake Passage the ratio is found to be 67.6 ± 1.3% [Sokolov et al, 2004] for four CTD occupations or 0.60 ± 0.02 for six CTD occupations [A. C. Naviera Garabato, pers. comm.]. In a study by Rintoul et al. [2002] the ratio is 65.8 ± 2.1% for six CTD occupations of the SR3 transect south of Tasmania.

6. Meridional baroclinic transport distribution

We now present results on the distribution of baroclinic transport over the meridional extent of the GoodHope section and show the contribution of transport within each frontal domain. The latitudinal distribution of the across section cumulated baroclinic transport for each repeat XBT section is shown in Figure 16. It is evident that throughout the sections there are anomalous periods of westward flow over small spatial ranges. The most prominent of these westward flows are located at the northern end and can be attributed to Agulhas Rings (refer to Section 3). This occurs during the third and fifth GoodHope transects, where eddies were identified in the temperature sections (refer to Figure 4). The most prominent of these was crossed during the third GoodHope transect and which produces large opposing baroclinic transports of 34 Sv westward at 41.5°S and 46 Sv eastward at 42°S. The magnitude of these transports supports the view that this feature is an Agulhas Ring, which has invaded the northern part of the ACC. Similar transport features have been recorded by surface drifters and subsurface floats (at approximately 800 m depth) in the region of 41°S [Richardson, 2007].

The mean baroclinic transport, for five GoodHope XBT transects, has been divided into half a degree latitudinal bands over the ACC extent (Figure 17a). Again, it is evident that the mean flow at the northern end of the section (north of 42°S) is found to have a strong mean westward flow. The mean westward flow north of 42°S is 6.1 Sv. Two broad peaks of eastward baroclinic transport are found between the latitudinal ranges of the SAF and APF (arrow ranges in Figure 17). The local maximum in eastward flow at the 52.5°S band is associated with the sACCf. There is little mean additional eastward baroclinic flow (<1 Sv) south of the sACCf and at the SBdy.

The meridional distribution of variability in the baroclinic transport (Figure 17b) is the highest in the region north of ~42.5°S due to the east-west fluctuations in flow associated with the meandering STF and intruding Agulhas eddies. In this region, the standard deviation exceeds 12 Sv. Large standard deviations are also found over the SAF, SAZ and the APF and may reflect either meridional shifts in the frontal positions, changes in current strength, and/or eddy genesis and activity. This was similarly shown to be the case along the SR3 and SURVOSTRAL sections completed south of Tasmania [Rintoul et al., 2002].

South of 51°S, the variability is, as expected, substantially less (standard deviations less than 3 Sv), where the gradient in dynamic height, over the southern most ACC fronts (sACCf and SBdy), is substantially less than those to the north (SAF and APF), therefore, transport variations in these fronts constitute lower standard deviations.

The baroclinic transports associated with the three inner ACC fronts (SAF, APF and sACCf), and their contribution to the net ACC baroclinic transport are calculated for each GoodHope transect and displayed in Table 3. This was done by accumulating the baroclinic transport between the point where the baroclinic transport was found to be zero or flowing westward, to the south and north of the axial front position. This allowed us to estimate the baroclinic transport directly related to the position of the front, located using the temperature criteria of Orsi et al. [1995]. The integration limits are indicated on Figure 15 for each of the three inner ACC fronts. The XBT-inferred frontal contributions largely match those deduced from the CTD sections. The contribution from the SAF and sACCf for the XBT-inferred baroclinic transports are 5.4% and 4.5% less, respectively. An overwhelming fraction (72%) of the net ACC baroclinic transport is accounted for by the three inner ACC fronts of which the SAF and APF dominate with a 32% and 28% contribution, respectively. This emphasises the key role the fronts play in determining the total baroclinic transport of the ACC.

Legeais et al. [2005], reveal that the sACCf contributes more to the net ACC transport (21%) than this study shows (11%). Legeais et al. [2005], make use of polynomial fits to estimate the baroclinic transport from XBT data. This type of fitting is significantly less precise at following the undulations in dynamic height linked to each front, which may be responsible for over-estimating the contribution made by the sACCf. In addition, the dynamic height gradient from XBT data obtained before 2004 seems to be somewhat greater between 52-55°S, than the most recent XBT data (see Figure 11). This would, in part, be responsible for the higher sACCf transport contributions made by Legeais et al. [2005].

Both the SAF and APF are primarily responsible for the variability associated with the total transport of the ACC. These two fronts have large baroclinic transport ranges, which exceed 20 Sv (SAF: 21.7-42.9 Sv; APF: 15.9-34.4 Sv), and their standard deviations are 8.8 Sv and 7.4 Sv (or 9%), respectively. The transport contribution of the STF and SBdy constitutes only a small fraction of the total transport, with each front contributing 4.4% and 1.3%, respectively. A large proportion of the remaining 22% of the total baroclinic transport may be accounted for by additional ACC jets, which are not taken into account when using the integration method used in this section. There are instances when a front appears to be separated into two or more branches of flow. The first GoodHope XBT transect provides such an example. The transports associated with the APF seem to be split into two distinct jets. One of these is located over the temperature front (~49°S) and the other at ~50°S, with a region of westward flow in-between the two eastward flowing jets. These additional transport jets are discussed in more detail in Section 7.

7. Baroclinic transports inferred from satellite altimetry data

An aim of this paper is to show that baroclinic transport estimates of the ACC, at a substantially improved temporal resolution, can be achieved. Hydrographic data are collected in the Southern Ocean primarily in the summer months, which creates the risk of aliasing high frequency variability. Annual XBT and CTD 'snapshot' sampling are not frequent enough to resolve the substantial ACC baroclinic transport variability that can be expected at smaller temporal scales. A continuous time series of absolute dynamic topography (ADT), at weekly intervals, between 1992-2007, is created. This is done by adding the altimeter sea level anomalies (multi-mission gridded SSH product from AVISO; see Section 2.3.1) to the mean surface dynamic height, relative to 2500 dbar, calculated from two CTD and five repeat GoodHope XBT sections. The gradient of the ADT compares closely with the CTD (Figure 18) and XBT dynamic height gradients. The ADT product is somewhat 'smoother' than the hydrographic dynamic heights and in some cases mesoscale features are less well resolved. The hydrographic dynamic height estimates are relative to 2500 dbar and include only the baroclinic signal above this level. The altimeter derived ADT, however, may reflect changes in the density field below 2500 dbar. Differences between the ADT and hydrographic dynamic heights may, therefore, in part originate from the baroclinic field below 2500 dbar, and the barotropic field. Without an accurate estimate of the geoid, we are unable to separate the baroclinic and barotropic components of the satellite altimeter measurements. The differences may also reflect temporal and spatial sampling discrepancies, mapping errors and tides which have not been entirely removed from the altimeter signal, as well as sampling errors incurred in attaining the CTD and XBT data. Similarly, this was the case when SSH anomalies, inferred from CTD and altimeter measurements, were compared south of Australia [Rintoul et al., 2002]. Despite these factors, hydrographic estimates of dynamic height and the ADT are very similar (mean RMSD is 0.063 dyn m). This suggests that the ADT largely reflects baroclinic changes in the upper 2500 m of the water column.

Before we attempt to estimate the baroclinic transports from the full time-series of ADT data, we explain the method of defining the ACC spatial limits and ACC fronts, using satellite altimeter products. Given that the ACC, south of Africa, is unbounded by any continental landmasses, it has an open ocean current structure. This becomes an advantage when estimating baroclinic transports using satellite altimetry products because no flow is omitted that occurs too close to coastal areas where altimeter data becomes unreliable due to tidal errors. This problem was encountered by Rintoul et al. [2002] south of Tasmania, where the flow between 45°S and the Tasmanian coast was excluded due to near-coast altimeter limitations.

More recently, high resolution hydrographic and satellite sampling have revealed that the ACC consists of multiple branches or filaments, which merge and split and vary in intensity, along the circumpolar course [Hughes and Ash, 2001; Sokolov and Rintoul, 2007a; 2007b]. Analysis of the altimeter-derived surface velocity magnitude ($\sqrt{(u^2 + v^2)}$) and the MADT along the second GoodHope transect (Figure 19a) makes it clear that more than one velocity jet exists per ACC front. The highest gradients in the MADT are, as expected, located over the main velocity jets, identified by the vertical solid grey lines in Figure 19a. We supplement this with high resolution *in-situ* temperature data (Figure 19b) whereby CTD and XBT temperature data are combined to better resolve the finer horizontal thermal gradient found over the velocity jets identified in Figure 19a. The high resolution temperature data reveals that the velocity jets, identified in Figure 19a, associate closely with regions of strong thermal gradients. This is especially the case with the dominant velocity jets of the SAF and APF. This suggests we can determine the multiple jet structure of the ACC using high resolution temperature sections south of Africa, in addition to that already undertaken in a study south of Australia [Sokolov and Rintoul, 2007a]. A time series of altimeter-derived surface velocity magnitude and MADT along the GoodHope transect is presented in Figure 20. The isolines of MADT (thin black lines) closely follow the surface velocity magnitudes of the main ACC jets (surface colour plot). This means we can, with accuracy, follow specified isolines of MADT to locate the boundaries between each of the ACC fronts, except that of the STF. South of Africa, the STF experiences considerable spatial variability induced by the presence of eddies (see Section 3). This provides us with difficulty in defining the northern limit of the ACC using satellite altimeter data when we do not have information of the vertical thermal or salinity structure, provided by *in-situ* hydrographic sections. Figure 20 confirms that there are no consistent surface velocity jets or isolines of MADT to use to track the limits of the STF, but rather episodic surface velocity maxima consistent with the presence of eddies and front meandering. This forces us to limit the northern domain of the ACC to the northern boundary of the SAF when we use satellite altimeter data alone. The boundaries between each ACC front are overlaid onto the surface velocity magnitude and MADT data, in Figure 20, using thick black lines. The isolines of MADT, used to define the front boundaries, are given as follows: northern limit of the SAF = 1.35 dyn m, SAF-APF = 0.94 dyn m, APF-sACCf = 0.31 dyn m, sACCf-SBdy = 0.0 dyn m, southern limit of the SBdy =

-0.13 dyn m. The northern limit of the SAF and the limit between the SAF and APF experience the highest latitudinal variability (± 0.79-0.85°), while the limits of the sACCf and the SBdy experience the least latitudinal variability (± 0.35-0.38°). It must be noted that on certain occasions (late 1992, 2000, 2001, 2003 and 2005), the SBdy domain is invaded by sea-ice. During these short periods, we locate the southern limit of the SBdy as the mean location during the 14 year time series of latitudes. The mean position and associated standard deviations can be found in Table 4.

We use the empirical relationship between dynamic height and cumulative baroclinic transport to estimate the baroclinic transport of the ACC (relative to 2500 dbar) from the ADT data. To test this approach, we compare the baroclinic transport estimated from the ADT data and from five XBT occupations along the GoodHope track (Figure 21). Both the transports and the form of the two curves are well reproduced. The accumulation of baroclinic transport over the SAF and APF is particularly well represented. The station pair differences are generally less than 8 Sv but increase over sections that have a low station density. Sections with largely spaced stations cause more abrupt changes in the dynamic height over latitude (specifically the third GoodHope XBT section; Figure 21d). The mean RMSD between the two transport estimates is 7.1 Sv and 10.1 Sv for the CTD and XBT sections, respectively. Near the fronts (namely the SAF and APF), the ADT deduced baroclinic transport gradient is greater (i.e. greater transport gains with latitude). This may, in part, reflect the deep structure of fronts, which extend closer to the sea floor than the rest of the ACC regime, and which are responsible for a significant proportion of the ACC's net baroclinic transport (see Section 6). Other differences between the ADT and hydrographically derived baroclinic transports may be due to deep baroclinic flow (>2500 dbar), and mapping errors and tides, which have not been removed from the altimeter signal. The difference between the two curves may also be attributed to the barotropic component of the flow captured in the altimeter signal and which is reproduced in the ADT product. We are unable to accurately estimate the contribution the deep baroclinic flow, mapping errors and tides have on the dynamic height and transport residuals. We, therefore, are not able to estimate the barotropic component of the transport found in the altimeter signal. In recent times, there has been slow progress made in determining the barotropic flow of the ACC. A significant contribution to determining the absolute transport structure of the ACC will be made once we have the ability to measure the barotropic component in the satellite altimetry data.

8. Continuous time series of net ACC baroclinic transport

The ADT is used to estimate a 14 year continuous time-series of baroclinic transport, relative to 2500 dbar, over each front and the whole ACC extent (Figure 22; Table 5) by exploiting the empirical relationship in Figure 13. The baroclinic transports are cumulated for each of the fronts, using the limits defined in Section 7, and between the southern limit of the SBdy and the northern limit of SAF for the whole ACC sector. The time series extends, at weekly intervals, between October, 14, 1992 and May, 23, 2007. The combined transport contribution is only 1.8 ± 0.8 Sv for the SBdy and 8.7 ± 2.2 Sv for the sACCf. The SAF and APF are responsible for a much higher mean transport contribution. The SAF and APF contribute 33.3 ± 3.1 Sv and 40.9 ± 2.4 Sv, respectively. The mean baroclinic transport estimate (relative to 2500 dbar) for the ACC is 84.7 ± 3.0 Sv. This is on average 2.8 Sv lower than the mean baroclinic transport estimate inferred from the XBT data. This 'missing' transport can largely be attributed to the fact that we limit the cumulated transports to the northern limit of the SAF and not to the STF, as was done with the hydrographic derived baroclinic transports.

The SAF and APF are characterised by high frequency transport variability when compared to the sACCf and SBdy. The dynamic height gradient over the SAF and APF is considerably larger than the sACCf and SBdy. This means that changes in the dynamic height gradient over the southern most fronts leads to smaller transport variations. Additionally, a portion of the transport variability may be associated with the latitudinal variability of the front limits. The transport contribution by the APF is, on average, 7.6 Sv higher than the SAF. This is in contrast to the frontal contributions made by the XBT-inferred transport estimates. In order to avoid subjectivity, we only associate the transport contribution located either side of the axial front location from the XBT-inferred transports (see Section 6). This may, therefore, underestimate the transport contributions for fronts that have multiple transport jets, which seems to be the case for the APF. The SAF, on the other hand, is characterised as having one main core transport jet (and two smaller transport jets), so little transport contribution is missed using the method described in Section 6.

The mean latitudinal distribution and standard deviation of the baroclinic transports, between 1992-2007, are represented in Figure 23. The SAF contains one distinct transport core located at ~44°S. Two small transport jets can be seen to the north and south of the main jet. These are located at ~43°S and ~44.5°S. In contrast, the APF has three distinct transport jets. The most prevalent of these is located at ~50.8°S, followed by one at ~49°S, and the smallest jet located at ~48°S. The sACCf contains two main transport jets, which cores lie at approximately 51.5°S and 52.5°S, respectively. The small transport jet, located at ~55.5°S, is associated with the SBdy. Periodic occurrences of westerly transport are found at the

SAF and APF limit and in between the APF transport jets. This is likely caused by eddy shedding at the front and jet boundaries. The dominant transport standard deviations are found at the main jets of each front, which may reflect the meridional movement and change in current strength of these jets. The highest transport standard deviations, for the region, occur at the SAF. The SAF accounts for over 50% of the latitudinal transport standard deviations of the ACC. This suggests that the transport variations in the SAF are responsible for a large proportion of the spatial baroclinic transport variability related to the ACC. The APF accounts for 33% of the total transport variance per latitude. This means the APF is over 35% more stable than the SAF, when concerning latitudinal transport variability even though the APF has a greater overall baroclinic transport contribution to the ACC. The sACCf and SBdy follow suit with a contribution of 14% and 3% to the total standard deviation, respectively. The front contributions to the net baroclinic transport and standard deviation of the ACC are summarised in Table 5.

9. Summary

The exploitation of data is extremely important in the Southern Ocean, where it is especially hard to obtain due to its isolation and hostile environment. This study demonstrates how repeat CTD sections allow us to derive proxy techniques to determine the variability of the ACC, using XBT and remotely sensed data alone. These alternative methods are used to make accurate estimates of baroclinic transport with high spatial and temporal resolution.

First, we showed that a close correlation exists between upper ocean temperature and dynamic height. Surface dynamic heights were, therefore, derived from XBT profiles, which compared closely to the 'true' dynamic heights calculated from CTD data. The agreement between the two estimates were excellent and differences were small (mean RMSD <0.05 dyn m). These differences were highest towards the southern and northern end of the sections, where communication between several water masses containing different temperature and salinity signatures, was most extensive. The resulting dynamic heights showed close correspondence with the location of the ACC fronts (where local maxima in gradients were experienced). Additionally, the dynamic height data were accurate at resolving mesoscale features evident in the temperature sections.

A similar empirical relationship between surface dynamic height and cumulative baroclinic transport was used to derive, with minimal error, the baroclinic transport from all available XBT dynamic height profiles. These transports were found only to be, on average, 2.3% higher than the actual geostrophic measurements. The ratio between 2500 dbar and bottom referenced CTD transports was relatively constant

(67%), thereby allowing us to reference the XBT baroclinic transports to full depth. The mean baroclinic transport, relative to 2500 dbar, for 18 XBT sections was 90 ± 2.4 Sv, while the bottom referenced baroclinic transport estimate was 145 ± 3.9 Sv.

The mean distribution of baroclinic transport with latitude exhibited broad bands of eastward flow associated with the three inner ACC fronts. As expected, these fronts also contributed to extensive amounts of variability in the ACC flow. The most northern part of the sections displayed periods of extreme flow reversals contributing to the highest amounts of transport variability. These occurrences were attributed to south-westward propagating Agulhas Rings, which penetrated the northern domains of the ACC along the GoodHope transect.

The ADT data, over the ACC, was created by adding SSH anomaly data to a mean surface dynamic height. The ADT compared closely with dynamic heights from CTD and XBT data (mean RMSD of 0.063 dyn m). Similarly, we applied the ADT to the empirical relationship between dynamic height and cumulative baroclinic transport to obtain a 14 year time series of net baroclinic transport estimates for the ACC. Intense mesoscale variability, in the form of eddies propagating from the Agulhas Retroflection, made it difficult to accurately define the northern limit of the ACC. Instead, we chose to cumulate the baroclinic transports to the northern limit of the SAF in order to provide a more accurate account of the net ACC baroclinic transport. The altimetry derived mean baroclinic transport of the ACC, relative to 2500 dbar, was 84.7 ± 3.0 Sv. The transports estimated per front, show that the SAF and APF contribute the bulk of the ACC baroclinic transport (~88%), while the sACCf and SBdy add the remaining ~12%. The mean latitudinal distribution of the transports reveals that each front is characterised by multiple eastward flowing jets that together, make up the total circumpolar flow. Interestingly, the SAF was found to contribute over 50% of the baroclinic transport variability of the ACC, even though its net transport contribution to the ACC was 9% less than the APF. The use of satellite altimetry products, to identify the front limits, proves to be a valuable tool in accurately defining the role and contribution each front has in determining the total baroclinic transport and associated variability of the ACC.

As shown by Rintoul et al. [2002] and Sokolov et al. [2004], these proxy techniques are appreciably promising and justify added effort to refine them further. The progression of the GoodHope programme in coming years will improve these methods through supplementary hydrographic sections. These proxy techniques highlight the value remote sensing techniques have on monitoring the transport and associated variability of the ACC, in a data sparse and remote expanse, like the Southern Ocean.

Acknowledgments The successful completion of the hydrographic surveys would not have been possible without the invaluable assistance of the captains, officers, crew and scientists of the MV S.A. Agulhas and RV Akademik Sergey Vavilov. We are grateful to Silvia Garzoli and NOAA/OCO for their support to implement the XBT deployments in high density mode, to Molly Baringer and Qi Yao for their assistance in the quality control of the data at NOAA/AOML, and to Steven Cook, Robert Roddy, Craig Engler and Jim Farrington for their logistics support with XBT deployments. S. Swart especially thanks S. Speich for the support during a total of eight months stay at the Laboratoire de Physique des Oceans, UBO, France and J.-F. Legeais for technical assistance. The work presented here is supported by the South African National Antarctic Programme (SANAP) and the Russian Academy of Sciences (Grant Meridian Plus #18.17.3) through the provision of funds and facilities. The authors also thank Dr A. Sokov for his effort in helping implement this programme and the Alfred Wegener Institute for Polar and Marine Research for the partial provision of data used in this study. Lastly, we would like to thank three anonymous reviewers for their comments, which helped improve the manuscript.

References

Ansorge, I. J., S. Speich, J. R. E. Lutjeharms, G. J. Goni, C. J. Rautenbach, W. Froneman, M. Rouault, and S. Garzoli. 2004. Monitoring the oceanic flow between Africa and Antarctica. *South African J. Sci*., **101**, 29–35.

Baily, R., A. Gronel, H. Phillips, G. Meyers, and E. Tanner. 1994. CSIRO Cookbook for quality control of expendable bathythermograph (XBT) data. *Rep. No.* 220. CSIRO Marine Laboratories, Hobart, Australia. 75 pp.

Belkin, I. M. and A. L. Gordon, 1996. Southern Ocean fronts from the Greenwich meridian to Tasmania. *J. Geophys. Res.*, **101**, 3675-3696.

Boebel, O., J.R.E. Lutjeharms, C. Schmid, W. Zenk, T. Rossby and C. Barron. 2003. The Cape Cauldron: a regime of turbulent inter-ocean exchange. *Deep Sea Res. Part II,* **50**, 57–86.

Budillon, G. and S. R. Rintoul. 2003. Fronts and upper ocean thermal variability south of New Zealand. *Antarctic Science,* **15**, 141–152.

Byrne, D. A., D. L. Witter, D. R. Watts, N. R. Pettigrew, C. M. Duncombe Rae, and S. Baker-Yeboah. 2006. Interocean heat and salt transports from the Agulhas Leakage: First results from ASTTEX. Eos Trans. AGU, *Ocean Sci. Meet. Suppl.,* **87**(36): Abstract OS22C–03.

Cai, W. 2006. Antarctic ozone depletion causes an intensification of the Southern Ocean super-gyre circulation. *Geophys. Res. Lett.*, **33**, L03712, doi:10.1029/2005GL024911.

Daneshzadeh, Y-H. C., J.F. Festa, and S.M. Minton. 1994. Procedures used at NOAA-AOML to quality control real time XBT data collected in the Atlantic Ocean. *NOAA Tech. Memo*. ERL AOML-78, NOAA Atlantic Oceanographic and Meteorological Laboratory. 44pp.

de Ruijter, W. P. M., A. Biastoch, S. S. Drijfhout, J. R. E. Lutjeharms, R. P. Matano, T. Pichevin, P. J. van Leeuwen, and W. Weijer. 1999. Indian-Atlantic interocean exchange: Dynamics, estimation and impact. *J. Geophys. Res.*, **104**(C9), 20,885–20,910.

Ducet, N., P. Y. Le Traon, and G. Reverdin. 2000. Global high-resolution mapping of ocean circulation from TOPEX/Poseidon and ERS-1 and -2. *J. Geophys. Res*., **105**, 19,477–19,498.

Duncombe Rae, C. M. 1991. Agulhas retroflection rings in the South Atlantic Ocean: an overview. *South African J. Mar. Sci.*, **11**, 327-344.

Emery, W. J. and R. E. Thomson. 2001. Data analysis methods in physical oceanography: 2nd Edition Revised. Elsevier Science. Amsterdam, 640p.

Gille, S. T. 2002. Warming of the Southern Ocean since the 1950s. *Science,* **295**, 1275–1277.

Gladyshev, S., M. Arhan, A. Sokov, and S. Speich. 2007. A hydrographic section from South Africa southwestward to the southern limit of the Antarctic Circumpolar Current at the Greenwich meridian. *Deep Sea Res*., submitted.

Gordon, A. L. 1985. Indian-Atlantic transfer of Thermocline Water at the Agulhas Retroflection. *Science* **227**, 1030–1033.

Gordon, A. L. 1986. Inter-Ocean Exchange of Thermocline Water. *J. Geophys. Res.,* **91**, 5037–5046.

Gordon, A. L., and B. A. Huber. 1995. Warm Weddell Deep Water west of Maud Rise, *J. Geophys. Res.*, **100**(C7), 13,747–13,753.

Hughes, C. W. and E. R. Ash. 2001. Eddy forcing of the mean flow in the Southern Ocean. *J. Geophys. Res.*, **106**(C2), 2713-2722.

Legeais, J. F., S. Speich, M. Arhan, I. J. Ansorge, E. Fahrbach, S. Garzoli, and A. Klepikov. 2005. The baroclinic transport of the Antarctic Circumpolar Current south of Africa. *Geophys. Res. Lett.*, **32**, L24602, doi:10.1029/2005GL023271.

Lemke, P. 1992. WHP Cruise Summary Information: A12. Tech. Rep., Alfred Wegner Institut fuer Polar und Meeresforschung, Bremerhaven, Germany.

Le Traon, P. Y., P. F. Nadal, and N. Ducet. 1998. An improved mapping method of multisatellite altimeter data. *J. Atmos. Oceanic Technol.* **15**, 522-534.

Le Traon, P. Y. and F. Ogor. 1998. ERS-1/2 orbit improvement using TOPEX/POSEIDON: The 2cm challenge. *J. Geophys. Res*., **103**, 8045-8057.

Levitus, S. 1982. Climatological Atlas of the World Ocean, NOAA Professional Paper No. **13**, pp. 191.

Lutjeharms, J.R.E. 1996. The exchange of water between the South Indian and South Atlantic oceans. In: Wefer, G., Berger, W.H., Siedler, G. & Webb, D.J. (Eds.), The South Atlantic: Present and Past Circulation, Berlin, Heidelberg: Springer-Verlag, 125-162.

Orsi, A. H., W. D. Nowlin, and T. Whitworth. 1993. On the circulation and stratification of the Weddell Gyre. *Deep Sea Res. Part I*, **40**, 169–203.

Orsi, A. H., T. Whitworth, and W. D. Nowlin. 1995. On the meridional extent and fronts of the Antarctic Circumpolar Current. *Deep Sea Res. Part I,* **42**, 641–673.

Richardson, P. L. 2007. Agulhas leakage into the Atlantic estimated with subsurface floats and surface drifters. *Deep Sea Res. Part I,* **54**, 1361-1389.

Rintoul, S. R. 1991. South-Atlantic interbasin exchange. *J. Geophys. Res*., **96**, 2675–2692.

Rintoul, S. R., J. R. Donguy, and D. H. Roemmich. 1997. Seasonal evolution of upper ocean thermal structure between Tasmania and Antarctica. *Deep Sea Res. Part I,* **44**, 1185–1202.

Rintoul, S. R., S. Sokolov, and J. Church. 2002. A 6 year record of baroclinic transport variability of the Antarctic Circumpolar Current at 140°E from expendable bathythermograph and altimetry measurements. *J. Geophys. Res*., **107**(C10), 3155, doi:10.1029/2001JC000787.

Rintoul, S. R. 2006. The global influence of the Southern Ocean circulation. Proceedings of 8 ICSHMO, Foz do Iguaçu, Brazil, April 24-28, 2006, INPE, 1349-1354.

Rio, M.-H., and F. Hernandez. 2004. A mean dynamic topography computed over the world ocean from altimetry, in situ measurements, and a geoid model. *J. Geophys. Res.*, **109**, C12032, doi: 10.1029/2003JC002226.

Roether, W., M. Samthein, T. J. Muller, W. Nellen, and D. Sahrhage. 1990. Sudatlantik- Zircumpolarstom, Reise Nr. 11, 3 Oktober 1989-11 Marz 1990, Meteor-Ber. 90-2. Tech. Rep., University of Hamburg, Hamburg, Germany.

SIO. 1985. Cruise Report: AJAX. Tech. Rep., Schripps Institution of Oceanography/Texas AM University, USA.

Sloyan, B. M., and S. R. Rintoul. 2001. Circulation, renewal and modification of Antarctic mode and intermediate water. *J. Phys. Oceanogr*., **31**, 1005– 1030.

Sokolov, S., B. A. King, S. R. Rintoul, and R. L. Rojas. 2004. Upper ocean temperature and the baroclinic transport stream function relationship in Drake Passage. *J. Geophys. Res*., **109**, C05001, doi: 10.1029/2003JC002010.

Sokolov, S., and S. R. Rintoul. 2007a. Multiple jets of the Antarctic Circumpolar Current south of Australia. *J. Phys. Oceanogr*., in press.

Sokolov, S., and S. R. Rintoul. 2007b. On the relationship between fronts of the Antarctic Circumpolar Current and surface chlorophyll concentrations in the Southern Ocean. *J. Geophys. Res.*, **112**, C07030, doi:10.1029/2006JC004072.

Speich, S., B. Blanke, and G. Madec. 2001. Warm and cold water routes of an OGCM thermohaline conveyor belt. *Geophys. Res. Lett.*, **28**, 311–314.

Speich, S., B. Blanke, P. de Vries, S. Drijfhout, K. Döös, A. Ganachaud, and R. Marsh. 2002. Tasman leakage: A new route in the global ocean conveyor belt. *Geophys. Res. Lett.*, **29**(10), 1416, doi: 10.1029/2001GL014586.

Speich, S. et al., 2007a. GOODHOPE/Southern Ocean: A study and monitoring of the Indo-Atlantic connections. Mercator Newsletter, October 2007, **27**, 29-41.

Speich, S., B. Blanke, and W. Cai. 2007b. Atlantic meridional overturning circulation and the Southern Hemisphere supergyre. *Geophys. Res. Lett.*, **34**, doi:10.1029/2007GL031583, 2007.

Sprintall, J., R. Peterson, and R. Roemmich. 1997. High resolution XBT/CTD measurements across Drake Passage. *WOCE Newsletters* **29**, 18-20.

Weijer, W., W. P. M. De Ruijter, H. A. Dijkstra, and P. J. van Leeuwen. 1999. Impact of interbasin exchange on Atlantic overturning. *J. Phys. Oceanogr.*, **29**, 2266– 2284.

Whitworth, T. and W. D. Nowlin. 1987. Water masses and currents of the Southern Ocean at the Greenwich meridian. *J. Geophys. Res.*, **92**, 6462–6476.

Table 1. Summary of the CTD sections used in this study

Section	Date	Ship	Institute	Chief Scientist
AJAX	Jan. 1984	R/V Knorr	Texas A&M U.	T. Whitworth
A21	Jan.-Mar. 1990	R/V Polarstern	U. Bremen	W. Roether
A12	May-Aug. 1992	R/V Meteor	A.W.I.	P. Lemke
SR2	Jan.-Feb. 1993	M/V SA Agulhas	U. Cape Town	M. I. Lucas
GH2	Nov. 2004	R/V Vavilov	Shirshov	S. Gladyshev
GH4	Oct. 2005	R/V Vavilov	Shirshov	S. Gladyshev

Table 2. Temperature criteria used to locate the ACC fronts, reproduced from Orsi et al. [1995]. STF is the Subtropical Front, SAF the Subantarctic Front, APF the Antarctic Polar Front, sACCf the southern ACC front, SBdy the southern boundary of the ACC and θ is potential temperature. The classical positions of the ACC fronts, along the GoodHope transect, as determined by Orsi et al. [1995], are given

Front	Temperature criteria	Classical position (°S)
STF	10°C < $\theta_{100\,m}$ < 12°C	39.9
SAF	θ > 4-5°C at 400 m, farther north	47.6
APF	θ < 2°C along θ_{min} at z < 200 m, farther south	49.6
sACCf	θ < 0°C along θ_{min} at z < 150 m, farther south	52.4
SBdy	Southern limit of vertical maximum of θ > 1.5°C, (~200m)	56.1

Table 3. Mean position of the three inner ACC fronts and associated contribution of each front to the XBT-derived baroclinic transport of the ACC (in Sverdrups and percentage of net ACC baroclinic transport, relative to 2500 dbar)

Front	Mean Position (°S)	Transport (Sv)	% Transport of ACC
SAF	44.6 ± 0.5	28.8 ± 8.8	32.3 ± 9.1
APF	50.4 ± 0.9	24.8 ± 7.4	28.4 ± 9.0
sACCf	52.8 ± 0.4	9.8 ± 5.9	11.1 ± 6.6
Total	-	63.4	72

Table 4. Mean position and standard deviation of the boundaries of each front, as defined using satellite altimetry

Front Boundary	Mean Position (°S)	Standard Deviation (° latitude)
STF-SAF	43.0	0.85
SAF-APF	47.4	0.79

APF-sACCf	51.9	0.57
sACCf-SBdy	54.9	0.35
southern SBdy	56.2	0.38

Table 5. Mean contribution of baroclinic transport by each front to the net baroclinic transport of the ACC derived from satellite altimetry data (in Sv and percentage, relative to 2500 dbar). The contribution of each front to the net transport standard deviation is given in percent.

Front	Transport (Sv)	% Transport of ACC	% of total standard deviation
SAF	33.3 ± 3.1	39.2 ± 2.5	50.7
APF	40.9 ± 2.4	48.4 ± 3.3	32.7
sACCf	8.7 ± 2.2	10.2 ± 2.6	13.6
SBdy	1.8 ± 0.8	2.2 ± 0.9	3.0

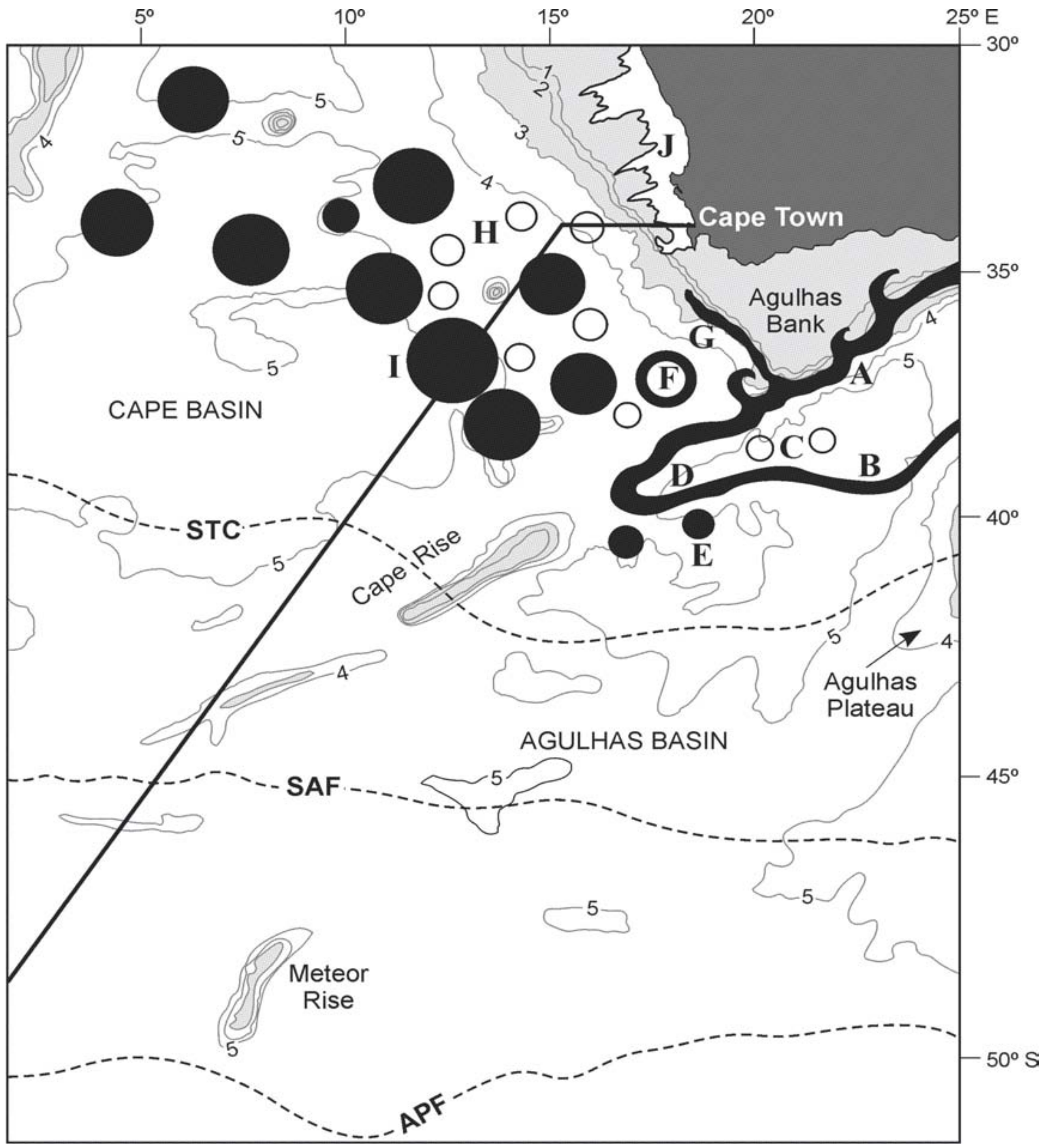

Figure 1. A conceptual diagram of the southern Agulhas Current system. Agulhas Rings (I) and filaments (G) are shed at the Agulhas Retroflection (D) and are carried equatorward by the Benguela Current (H). The Agulhas Current retroflects forming an eastward flow (B) to the north of the Subtropical Convergence (STC; otherwise known as the Subtropical Front). The GoodHope transect (solid line) crosses the southern domains of the Benguela upwelling regime (J). The STC, SAF and APF denote the mean locations of the Subtropical Convergence, Subantarctic and Antarctic Polar fronts, respectively. Bathymetry contours are in km and depths less than 300 m are shaded.

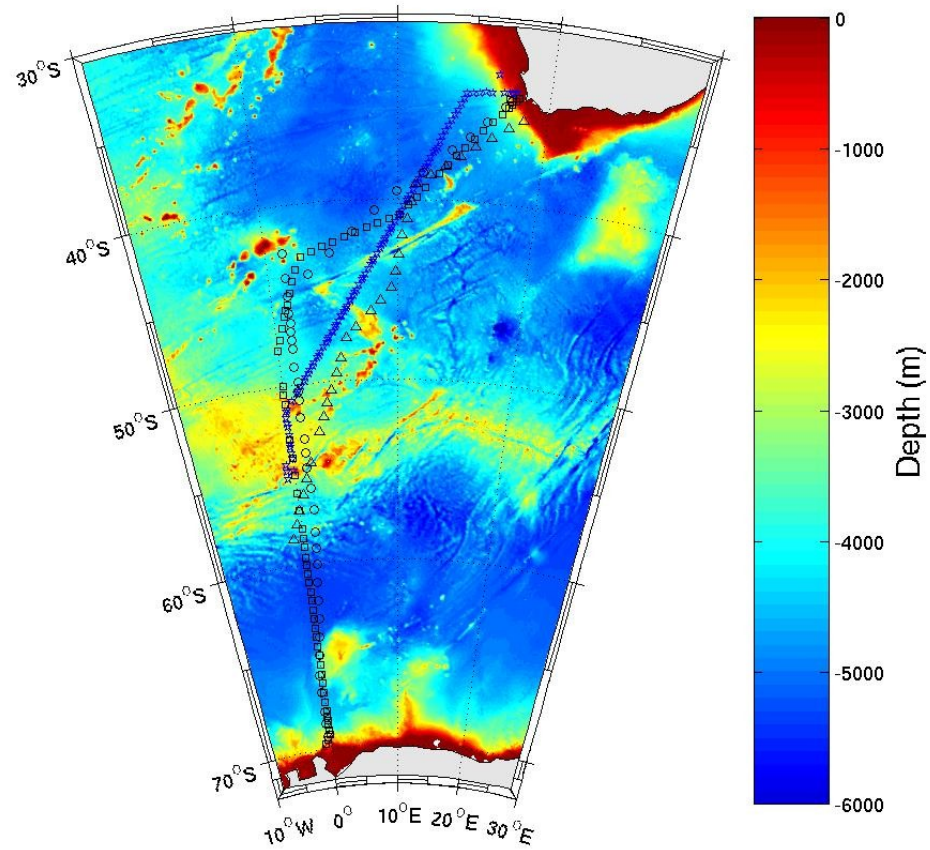

Figure 2. Locations of the six CTD sections used in this study (Table 1). The AJAX section (circles), A21 section (triangles), A12 section (squares), SR2 (diamonds), GoodHope 1 and 2 (stars). The section tracks have been overlaid on bathymetry (in meters).

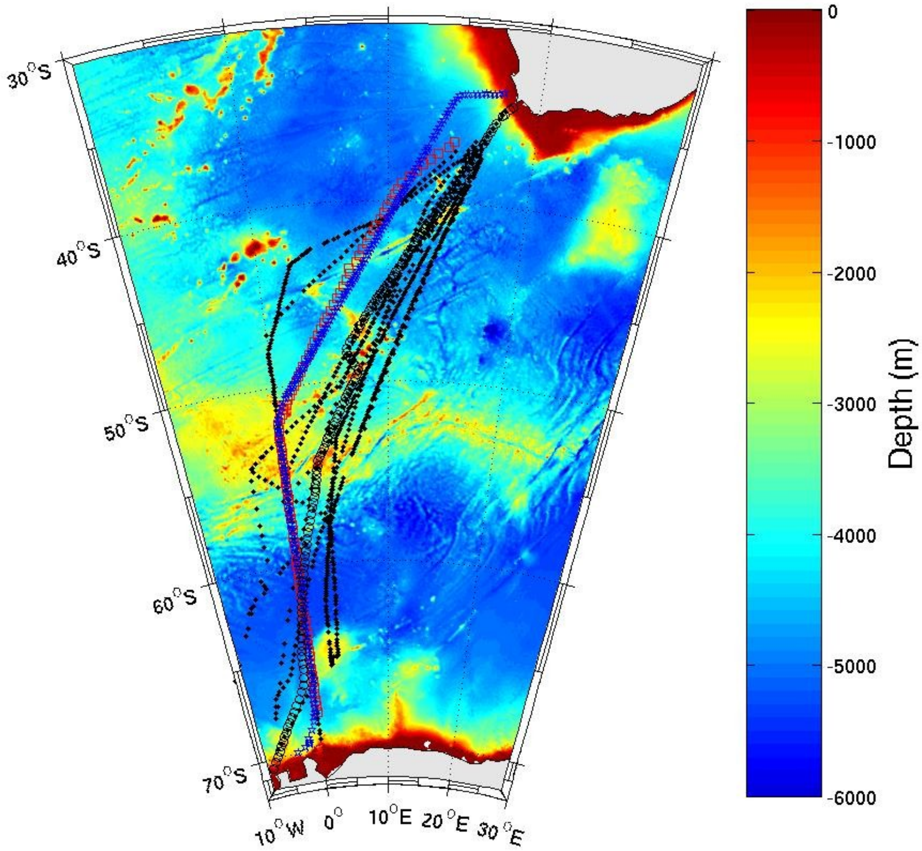

Figure 3. Locations of the XBT stations used in this study. GoodHope repeat section (stars), AARI section (squares), AWI sections (dots) and the AA-CT section (circles). The section tracks have been overlaid on bathymetry (in meters).

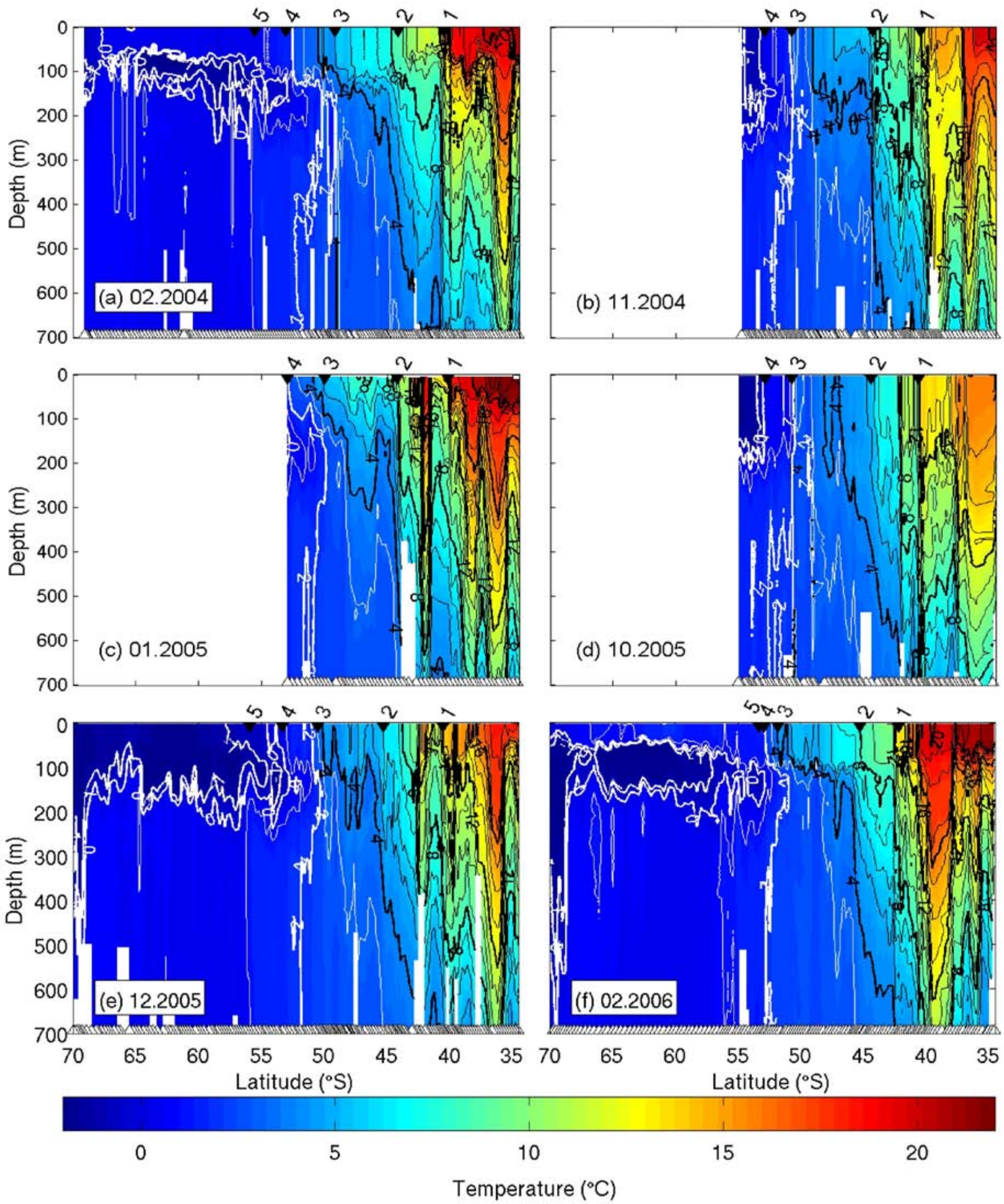

Figure 4. Temperature sections for the following transects: (a) GoodHope 1: February 2004, (b) GoodHope 2: November 2004, (c) GoodHope 3: January 2005, (d) GoodHope 4: October 2005, (e) GoodHope 5: December 2005, (f) Antarctica-Cape Town (AA-CT): February 2006. The black arrows show the latitudes of the ACC fronts (from north to south: STF (1), SAF (2), APF (3), sACCf (4), SBdy (5)). Triangles, along the bottom x-axis, indicate station positions. Note that the figures have equal axes of depth and latitude.

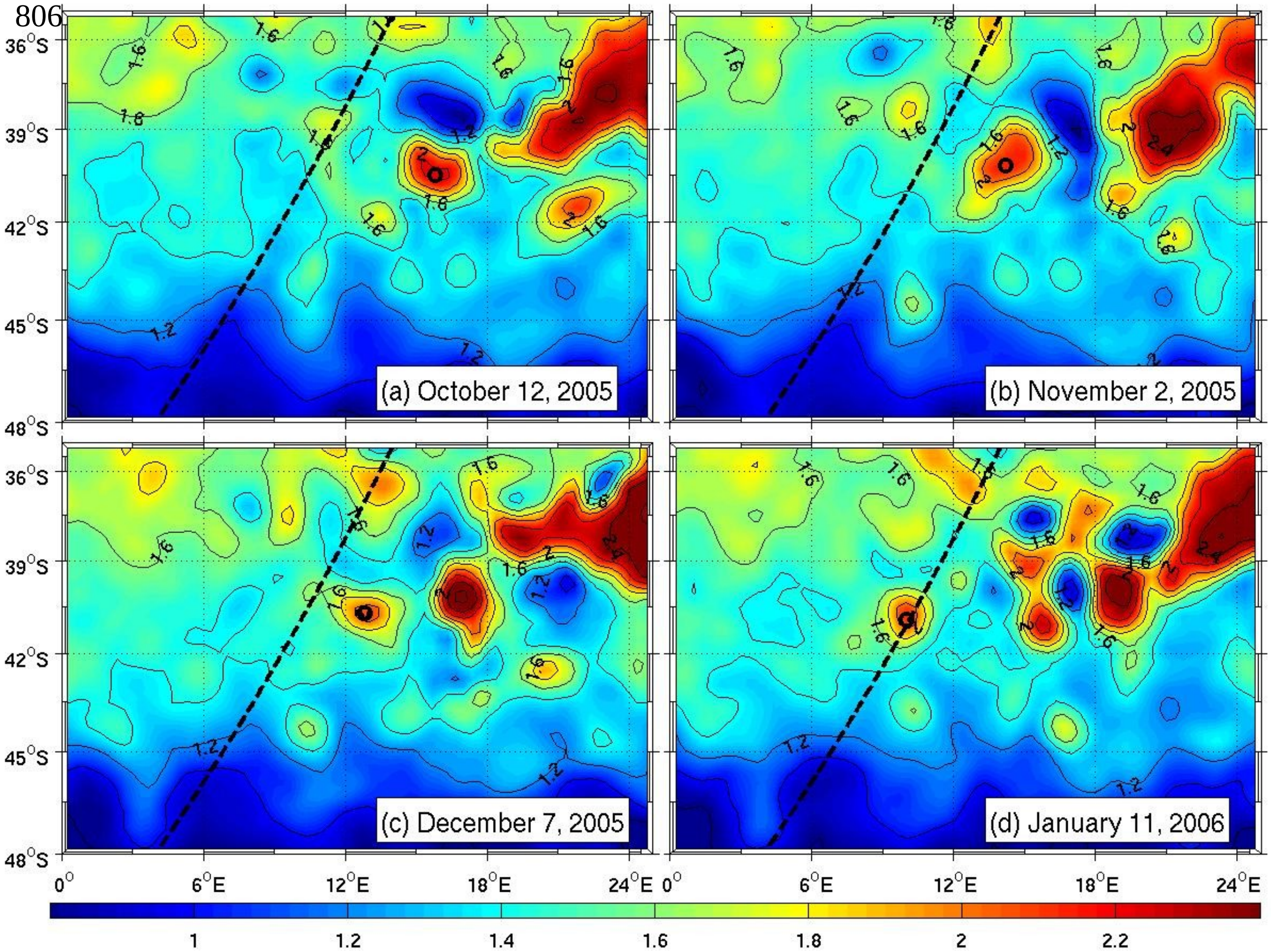

Figure 5. The MADT data (in dyn m) for the region located near the GoodHope cruise track between October 12, 2005 and January, 11, 2006. The propagation of an Agulhas Ring, marked with a black circle near its core, crosses the GoodHope cruise track (dashed line), at approximately 40°S.

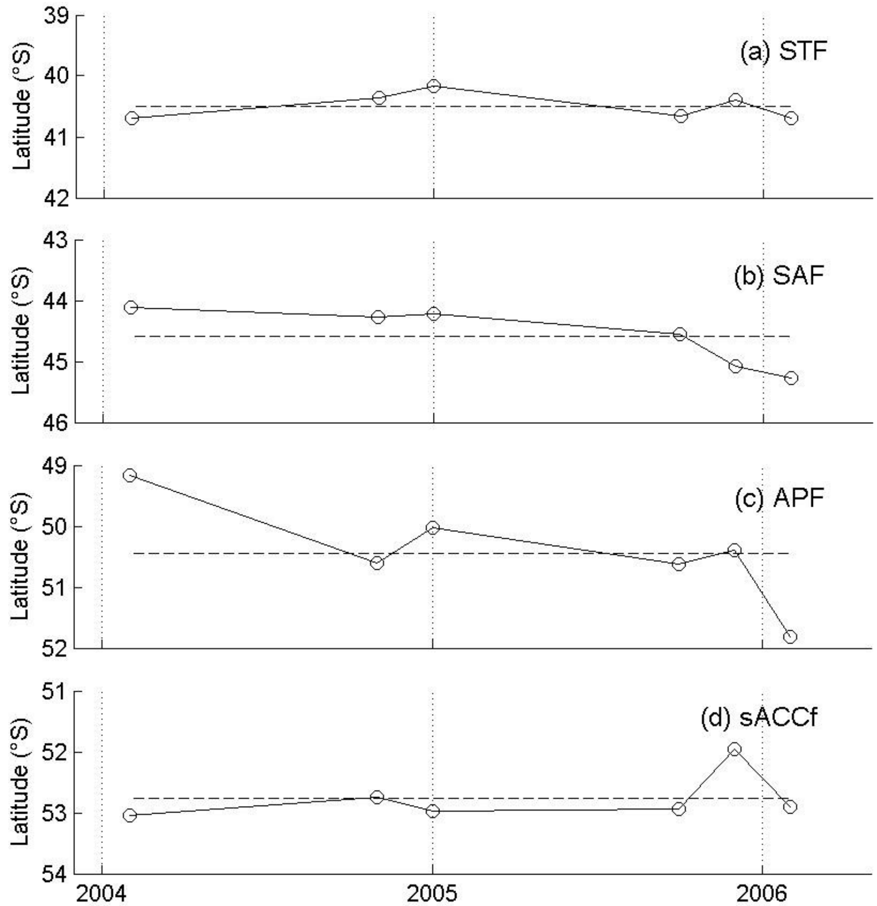

811**Figure 6.** Latitudes of the (a) STF, (b) SAF, (c) APF, (d) sACCf for the Africa to Antarctica transects
812completed between 2004-2006. The dashed line depicts the mean frontal position for six transects.

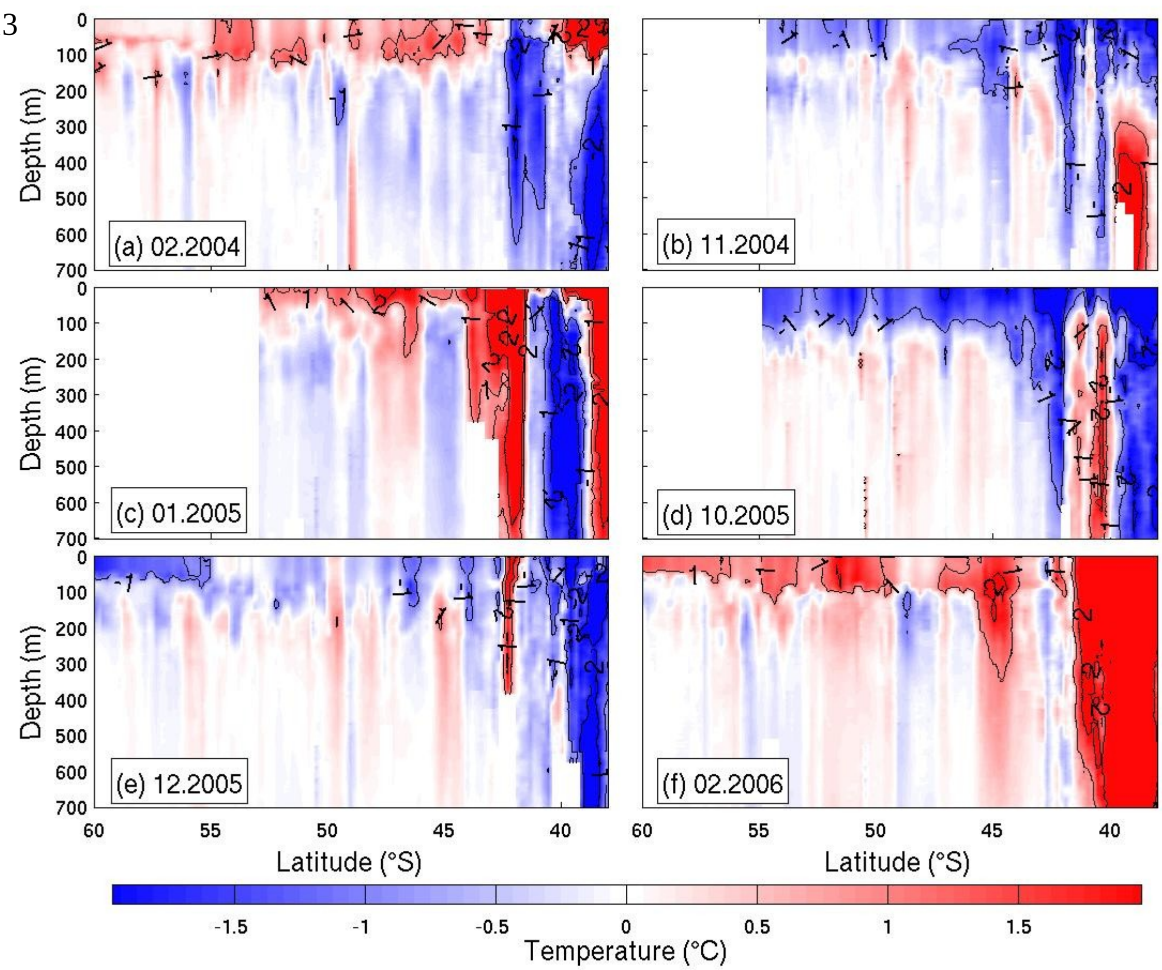

Figure 7: Temperature anomaly sections for the following transects: (a) GoodHope 1: February 2004, (b) GoodHope 2: November 2004, (c) GoodHope 3: January 2005, (d) GoodHope 4: October 2005, (e) GoodHope 5: December 2005, (f) Antarctica-Cape Town (AA-CT): February 2006.

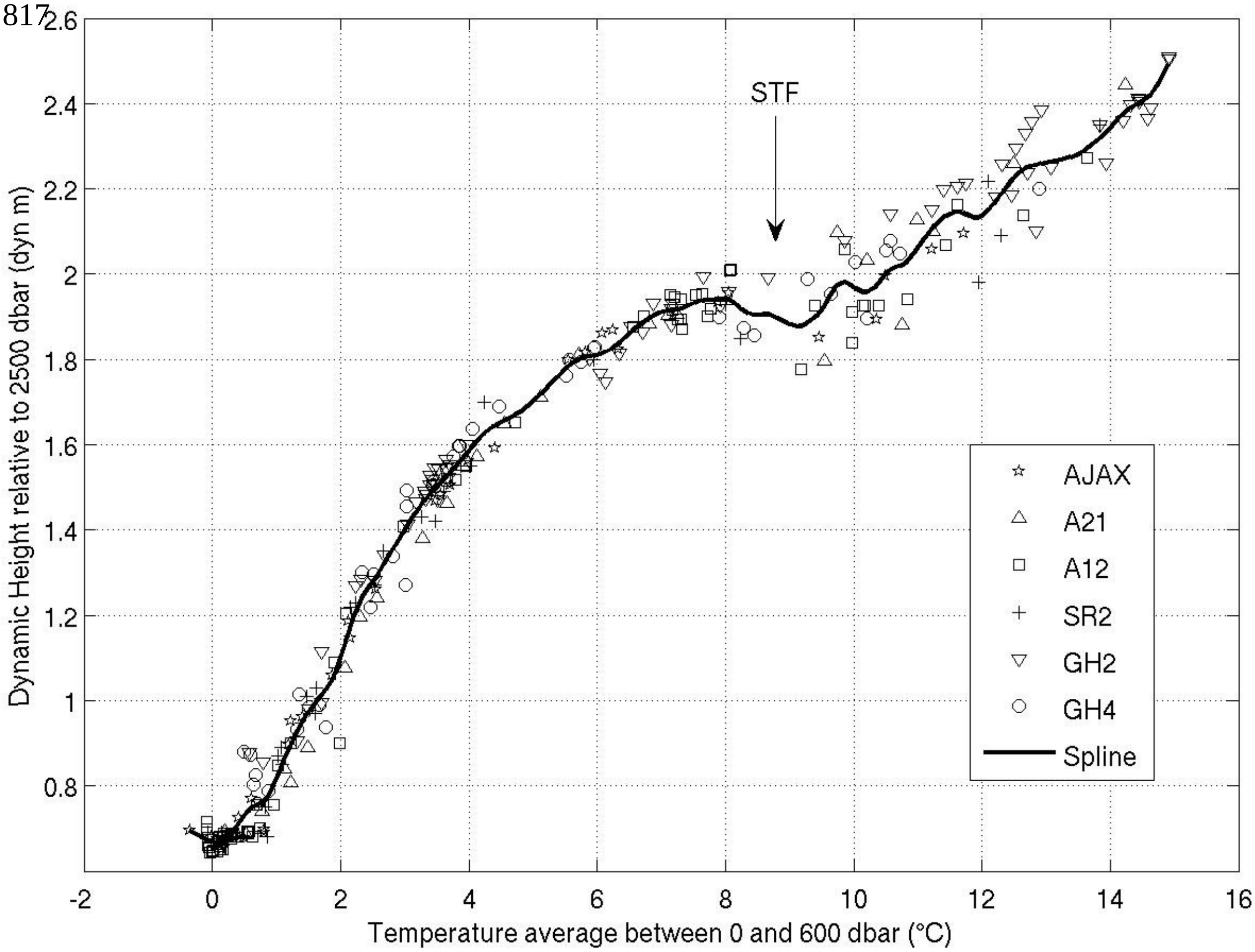

Figure 8. Dynamic height at the surface, relative to 2500 dbar, versus temperature averaged between the surface and 600 dbar. Data comes from six CTD transects completed in the south Atlantic: AJAX (stars), A21 (triangles), A12 (squares), SR2 (crosses), GH2 (down triangles), GH4 (circles). The solid curve depicts a smoothing spline fit to the data.

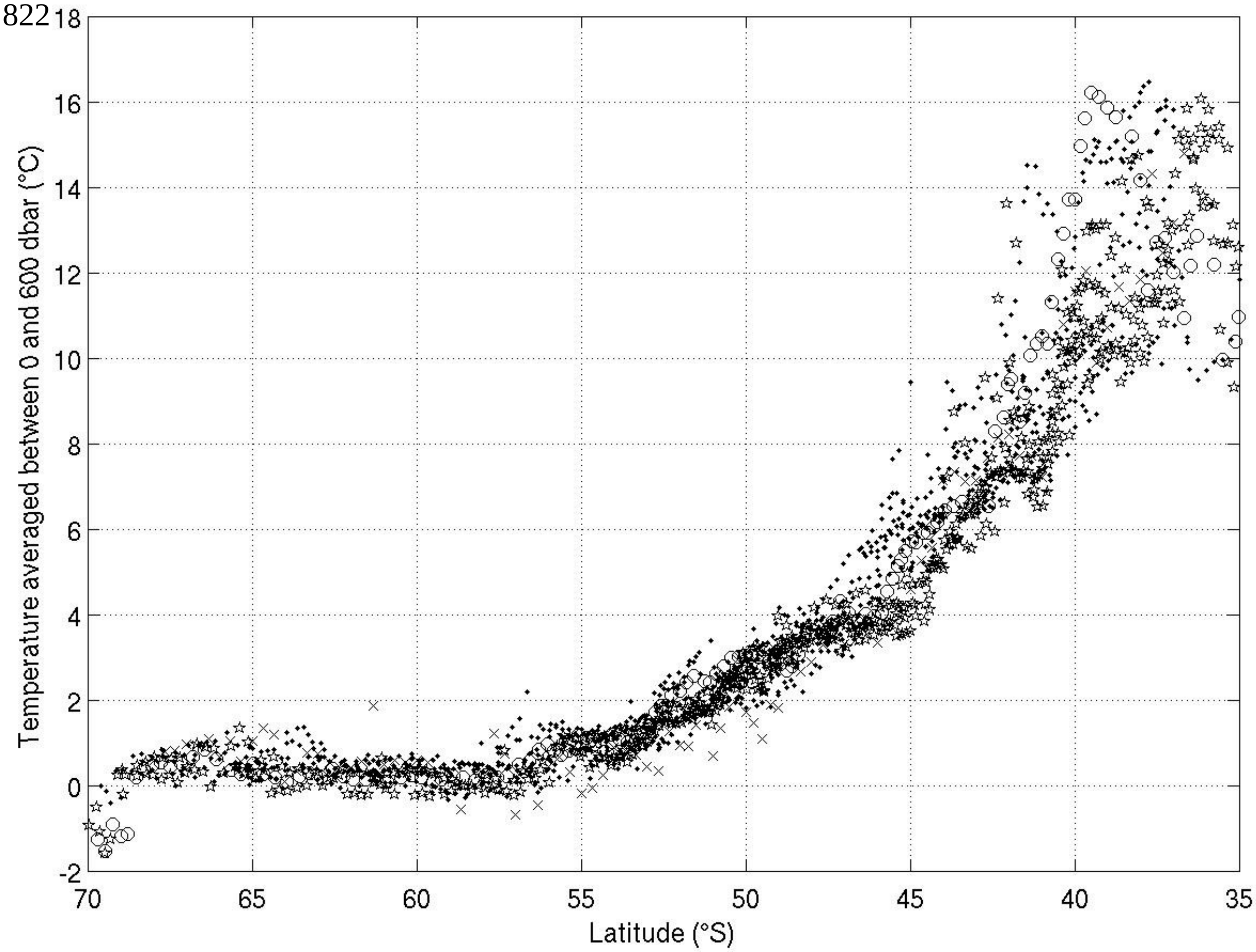

Figure 9. Average temperature, between 0 and 600 dbar, versus latitude for 18 XBT sections, completed in the South-East Atlantic. Data comes from repeat GoodHope sections (stars), AA-CT section (circles), AWI sections (dots) and an AARI section (crosses).

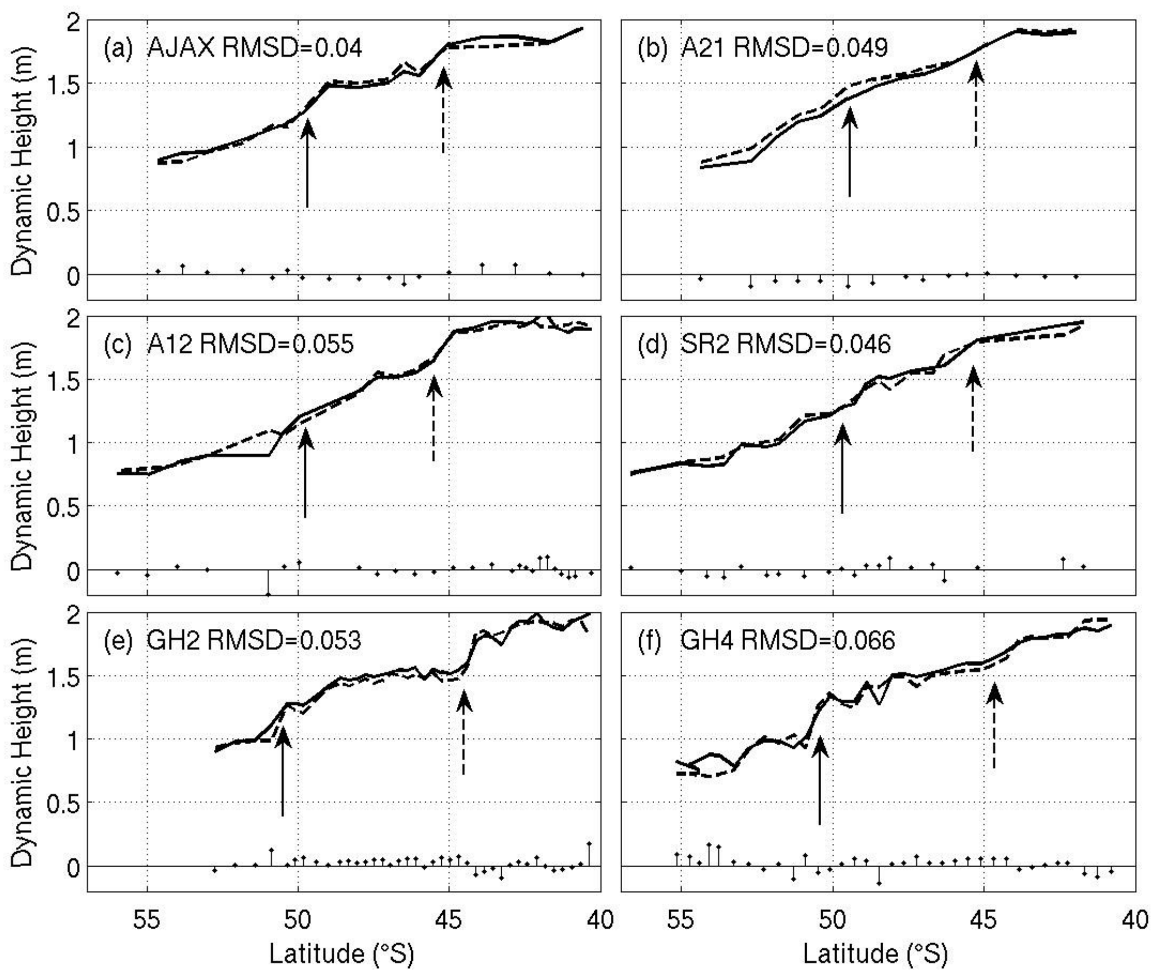

Figure 10. Comparison of 'true' dynamic height, above 2500 dbar (solid line), and dynamic height derived from the empirical relationship (dashed line) between upper ocean temperature and dynamic height in Figure 8. The dashed and solid arrows represent the positions of the SAF and APF, respectively. Differences between the two dynamic heights are shown along the x-axis. The RMSDs are given in dyn m.

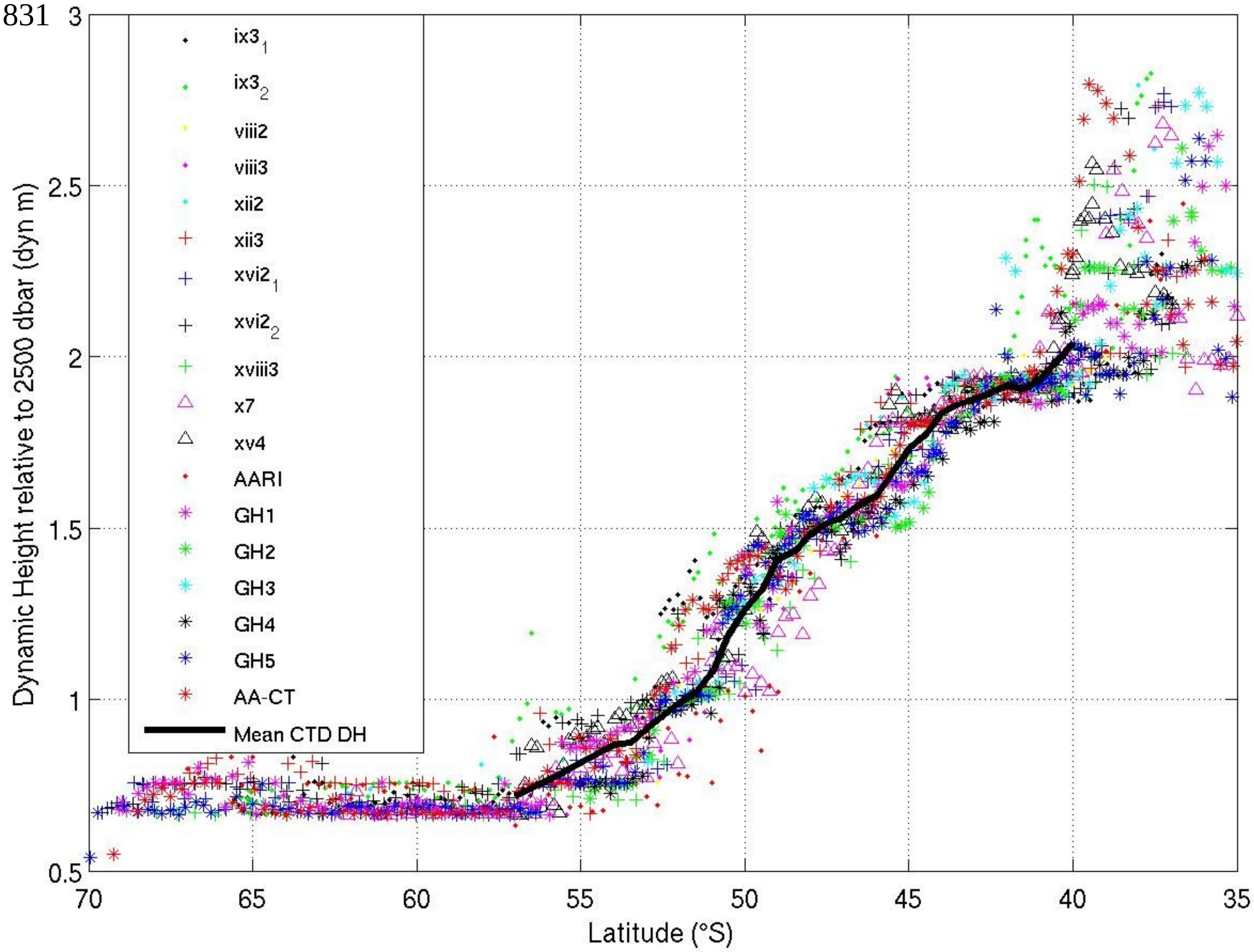

Figure 11. Dynamic height at the surface, relative to 2500 dbar, calculated using the empirical relationship in Figure 8, versus latitude for 18 XBT sections. The solid line represents the mean dynamic height calculated from temperature and salinity data from the six CTD transects.

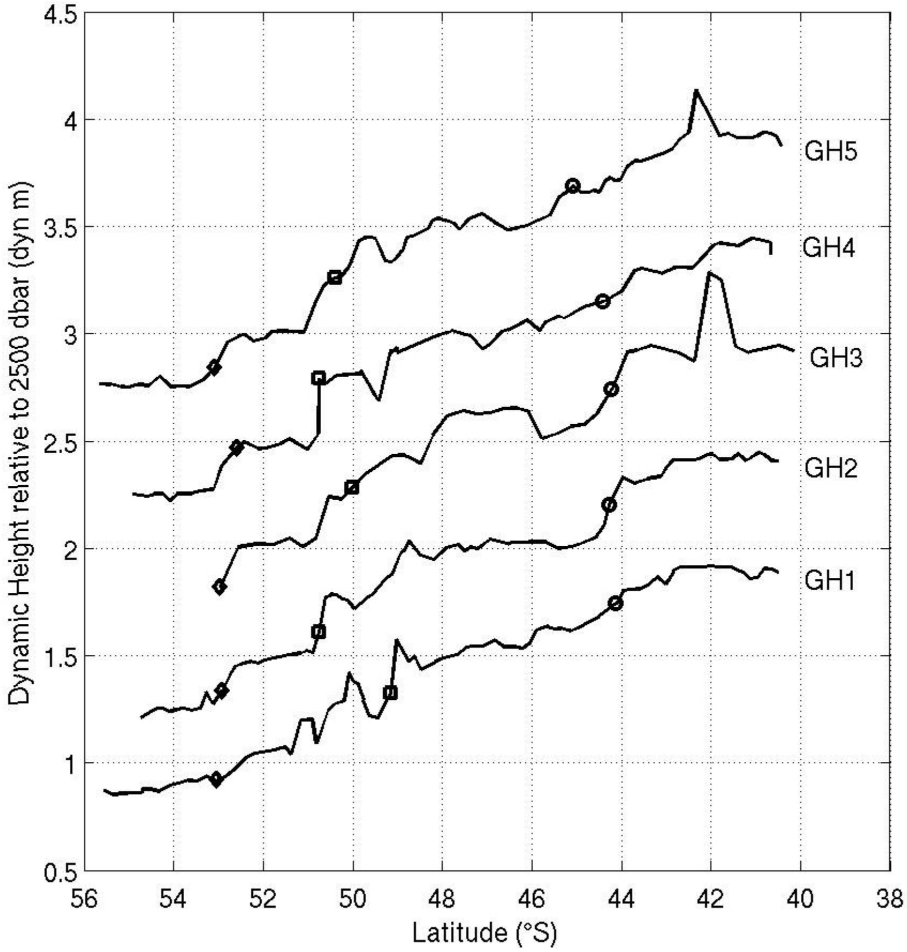

Figure 12. Dynamic height at the surface, referenced to 2500 dbar, for five repeat GoodHope XBT sections (2004-2006), estimated using the regression relationship in Figure 8. The estimated dynamic heights between sections are offset by 0.5 dyn m for clarity. The offset begins from the first section (GH1). The markers along each profile represent the latitudes (found using the temperature sections) of the SAF (circles), APF (squares) and the sACCf (diamonds).

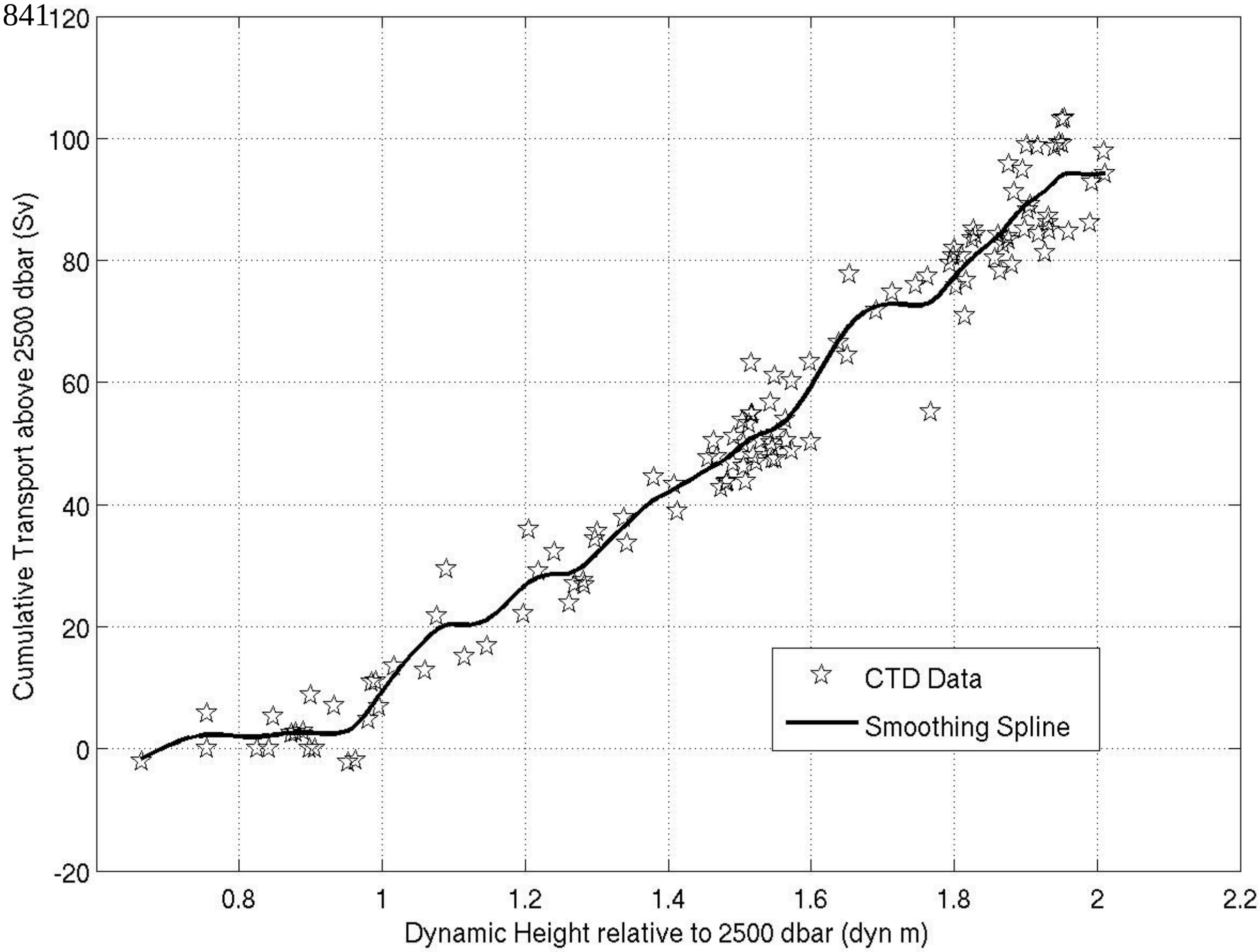

Figure 13. Northward baroclinic cumulative transport (above and relative to 2500 dbar) versus dynamic height at the sea surface, relative to 2500 dbar, of five CTD transects completed in the South-East Atlantic (including two occupations of GoodHope). The solid curve depicts a smoothing spline fit to the data.

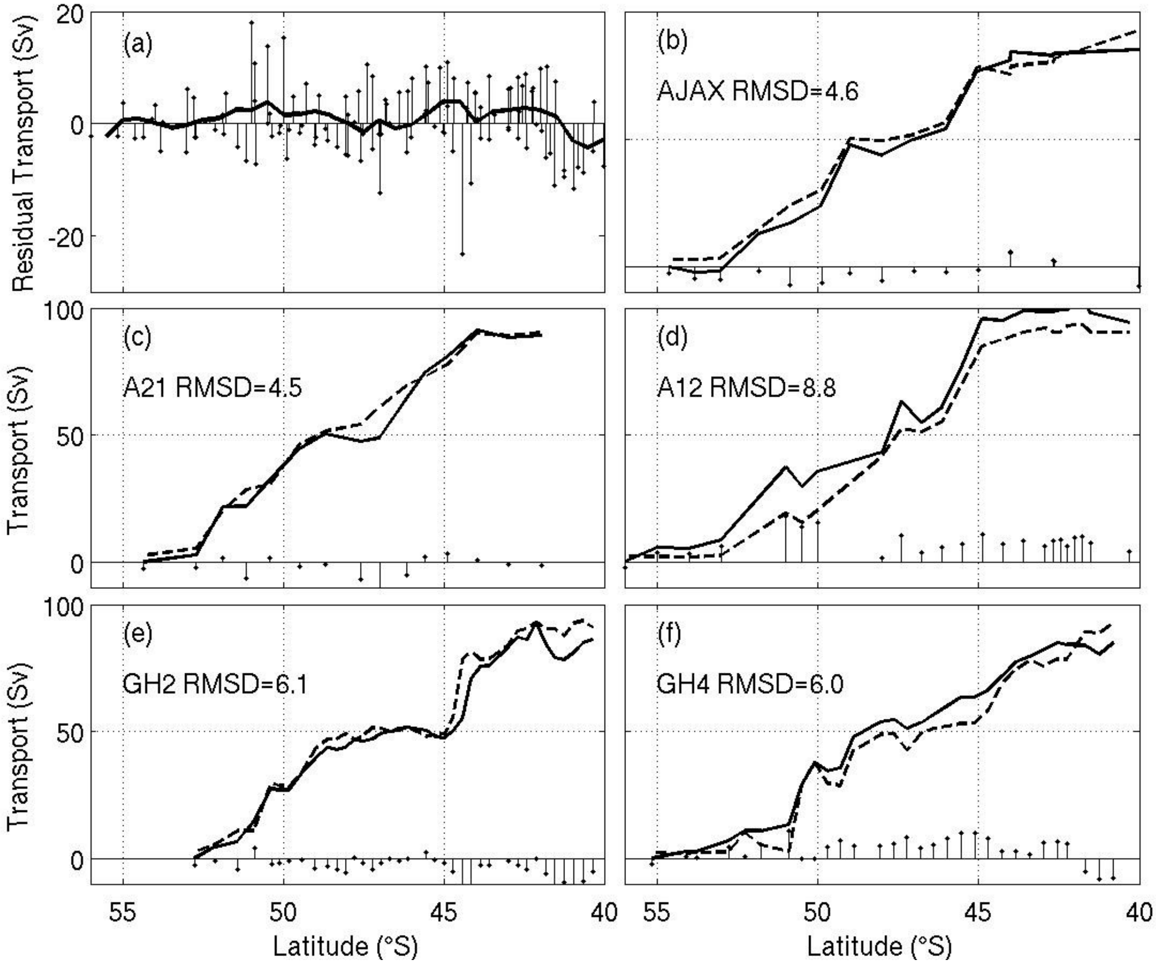

Figure 14. Comparison of baroclinic transport, relative to 2500 dbar (solid line), from CTD data, and baroclinic transport, derived from the empirical relationship (dashed line) in Figure 13. The comparisons are made from five CTD sections. Differences between the two transports are shown along the x-axis. The RMSDs are given in Sv. The differences between the curves (in Sv) are shown along the x-axis and are summarised in (a). The solid line, in (a), shows the mean residual plotted as a function of latitude.

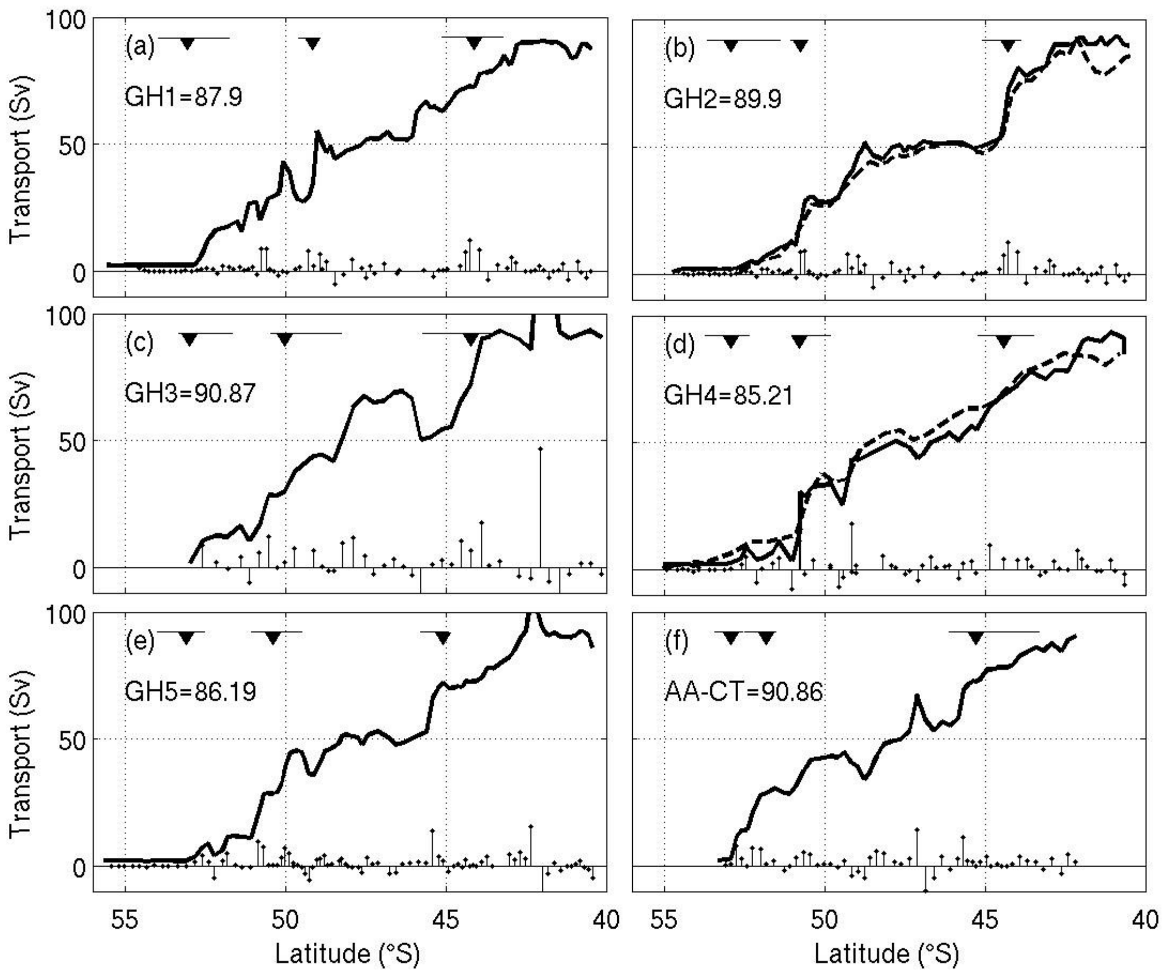

Figure 15. Northward cumulative baroclinic transport (referenced to 2500 dbar) for five repeat GoodHope XBT transects and the AA-CT section (bold line). The equivalent geostrophic transports from the CTD sections are shown for GoodHope 2 and 4 (dashed line). Differences in transport at each station pair are shown along the x-axis. The net cumulative baroclinic transport (in Sv) is given next to each section label. The positions of the three inner ACC fronts, determined from the temperature sections, are represented by the arrows (from south to north: sACCf, APF, SAF). The transport integration limits for each of these fronts is represented by the bar, placed above each arrow.

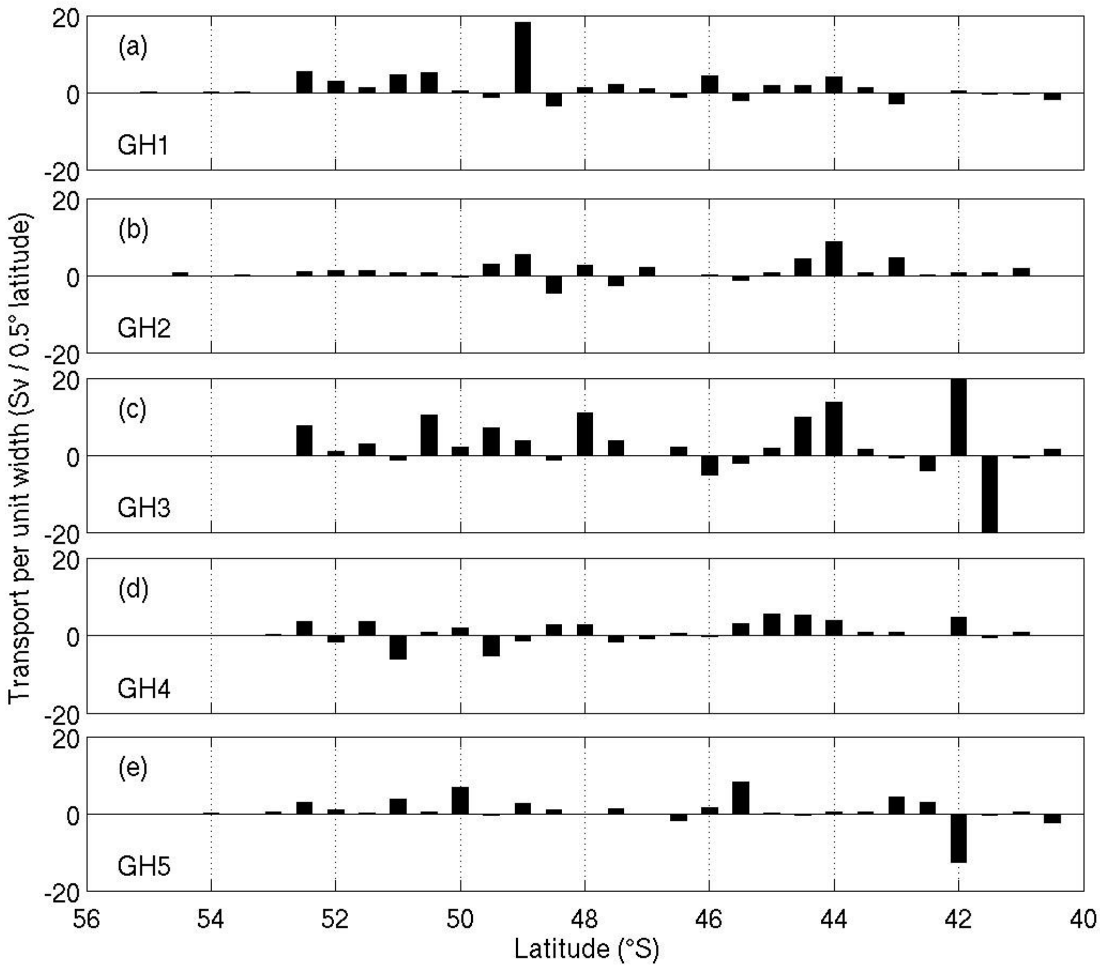

860**Figure 16.** Baroclinic transport across the GoodHope sections per half degree latitude for five repeat
861occupations of GoodHope. Eastward flow is positive.

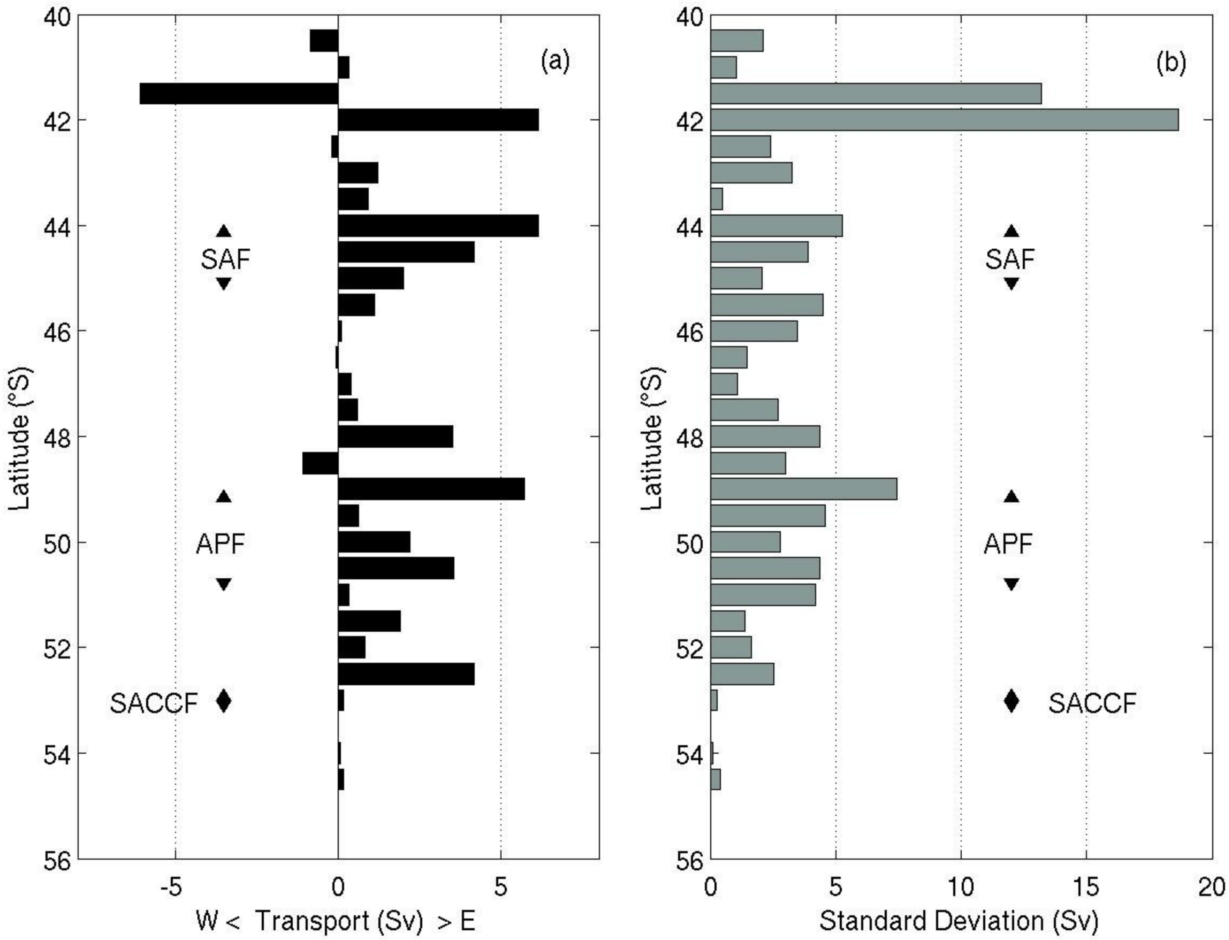

Figure 17. (a) Mean baroclinic transport, relative to 2500 dbar, per half degree latitude for five occupations of GoodHope. Eastward flow is positive. (b) The standard deviation of cumulative baroclinic transport for the half degree latitude bands is given. The arrows indicate the latitudinal range of the three inner ACC hydrographic fronts (SAF, APF sACCf), during five repeat GoodHope occupations.

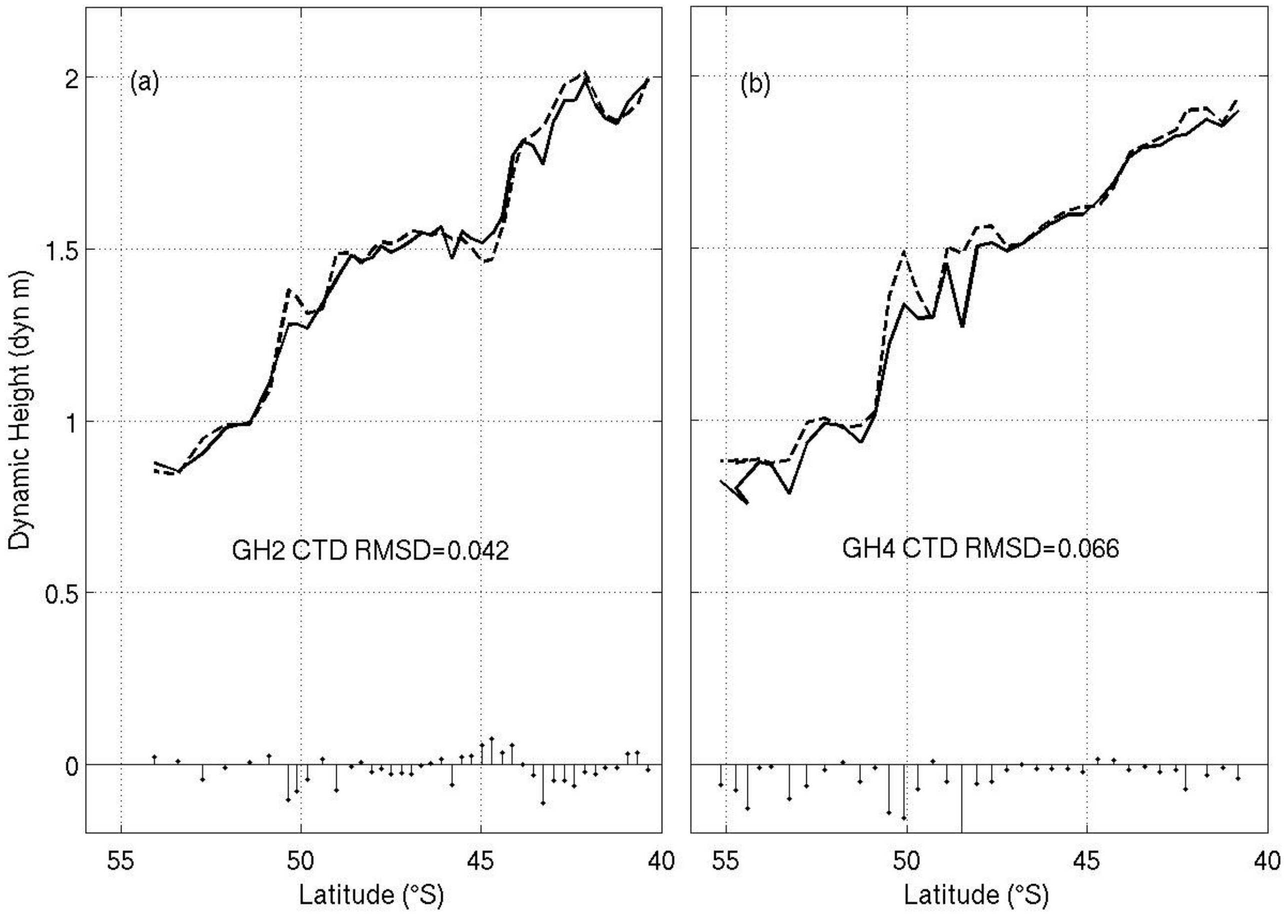

Figure 18. Comparison of surface dynamic height, relative to 2500 dbar, from CTD data (solid line) and from the ADT produced using altimetry data (dashed line), for two occupations of the GoodHope cruise track. The differences between the two estimates are shown along the x-axis.

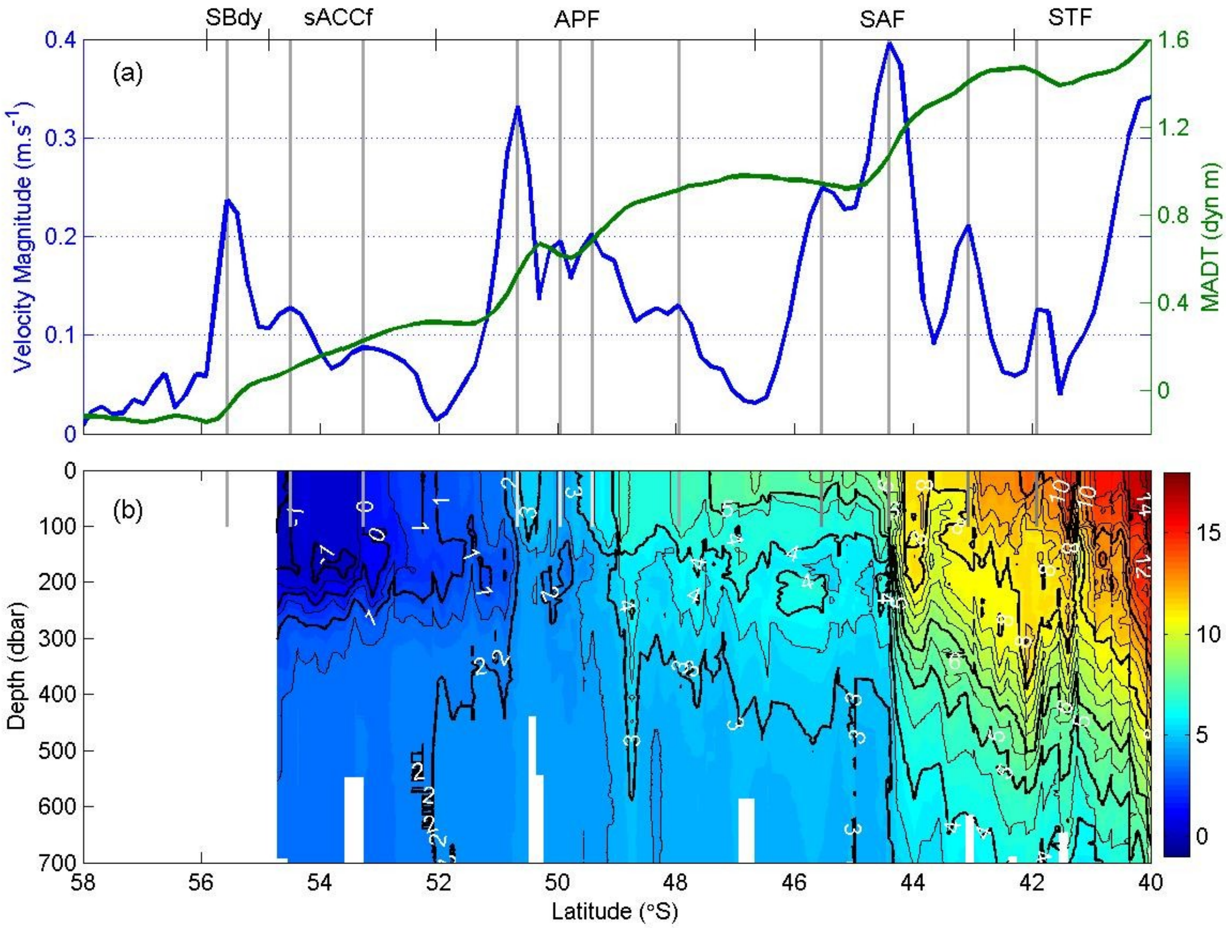

Figure 19. (a) Surface velocity magnitudes (solid blue line) and MADT data (solid green line) identify the transport jets (marked with vertical solid grey lines), associated with the ACC fronts. The proposed limits of each front, associated with this example, are indicated on the upper x-axis. (b) High resolution temperature data (combination of CTD and XBT temperature profiles; in °C) obtained during the second GoodHope crossing are used to show the vertical thermal structure associated with the transport jets identified in the upper figure panel.

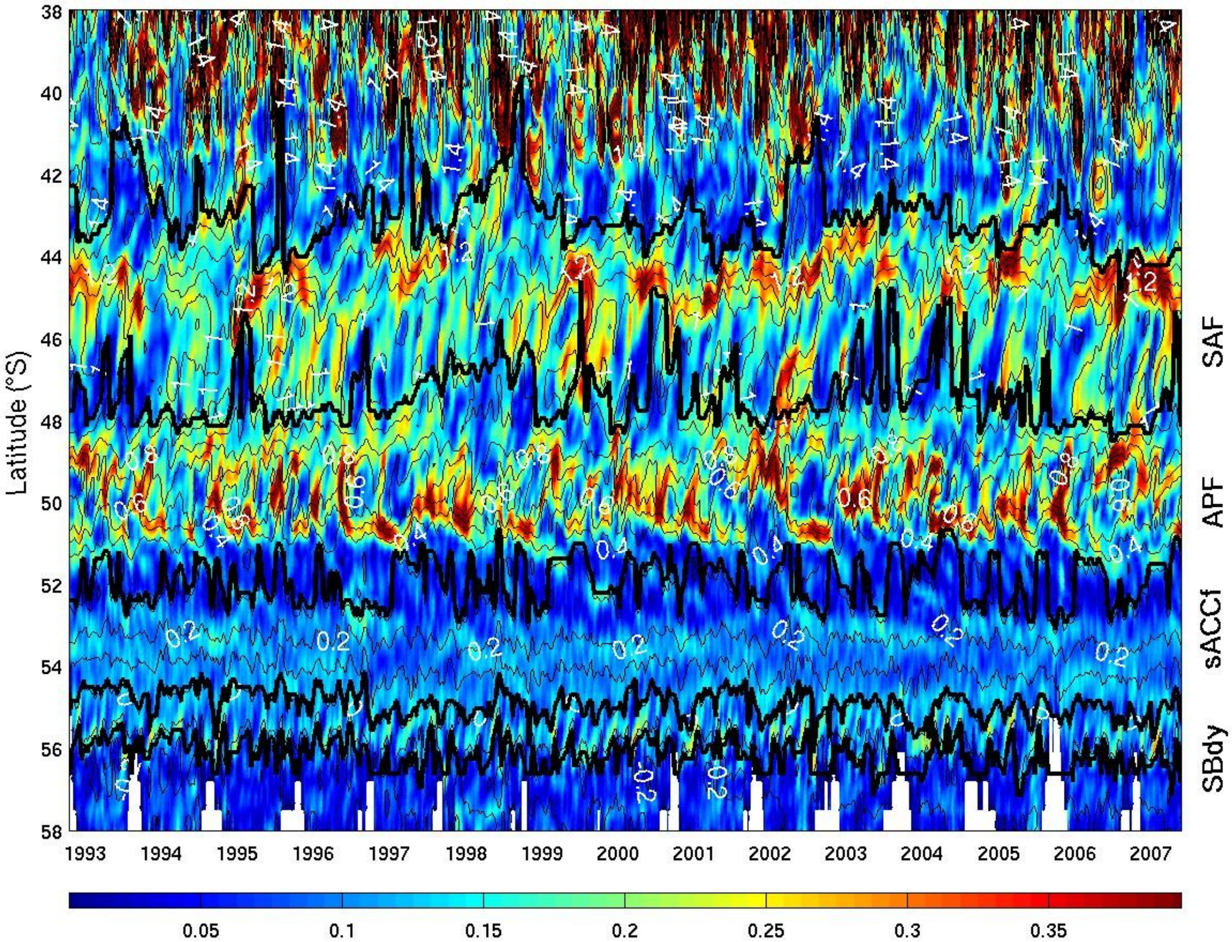

Figure 20. Time series of velocity magnitudes (colour surface plot; in ms^{-1}) and MADT (thin black lines; in dyn m) over the GoodHope cruise track. The boundaries between each ACC front (excluding the northern STF) are illustrated using the thick black lines.

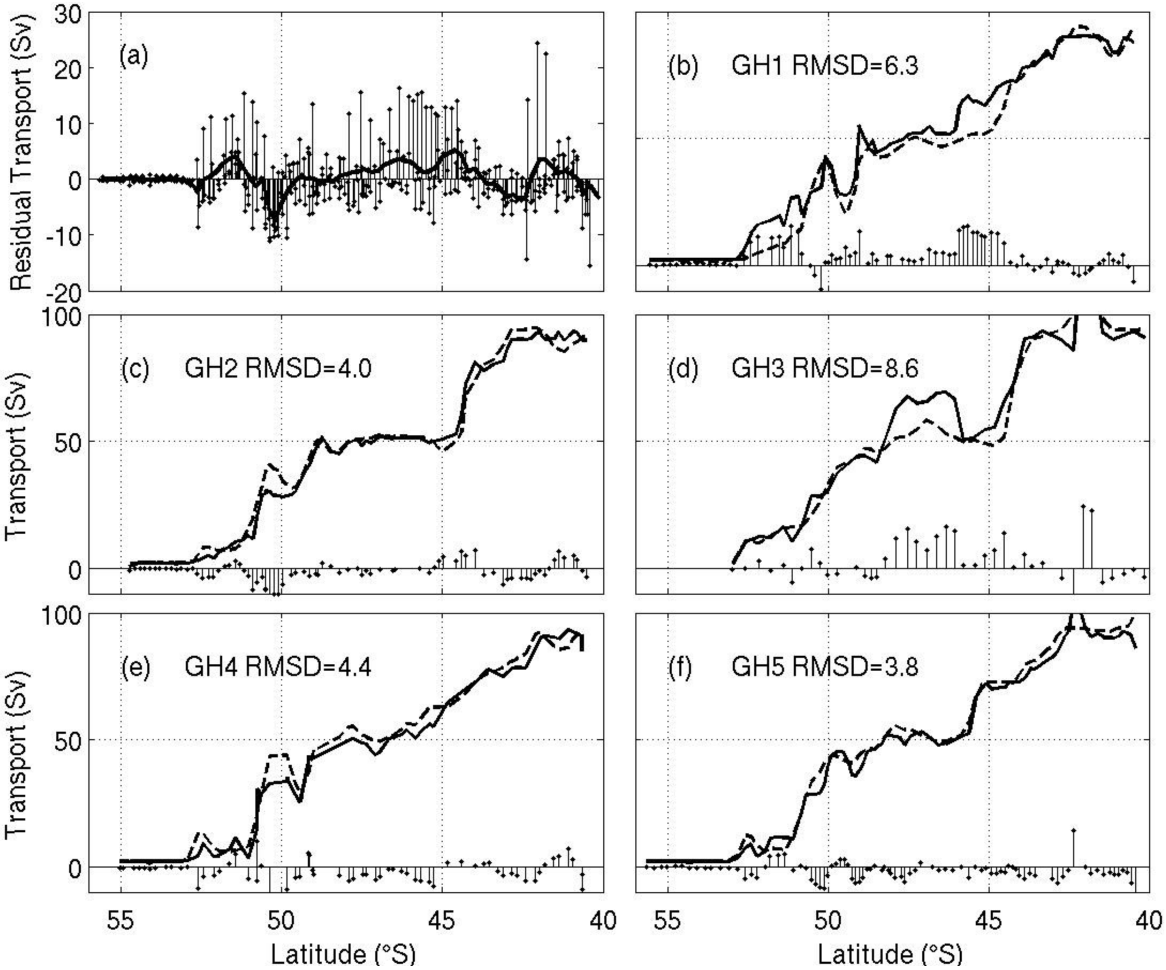

Figure 21. Comparison between baroclinic transport estimated from the ADT (dashed line) and from XBT dynamic height data (solid line; b through f), for five occupations of the GoodHope track. The differences between two transport estimates (in Sv) are shown along the x-axis and summarised in (a); the solid line is the mean residual plotted against latitude.

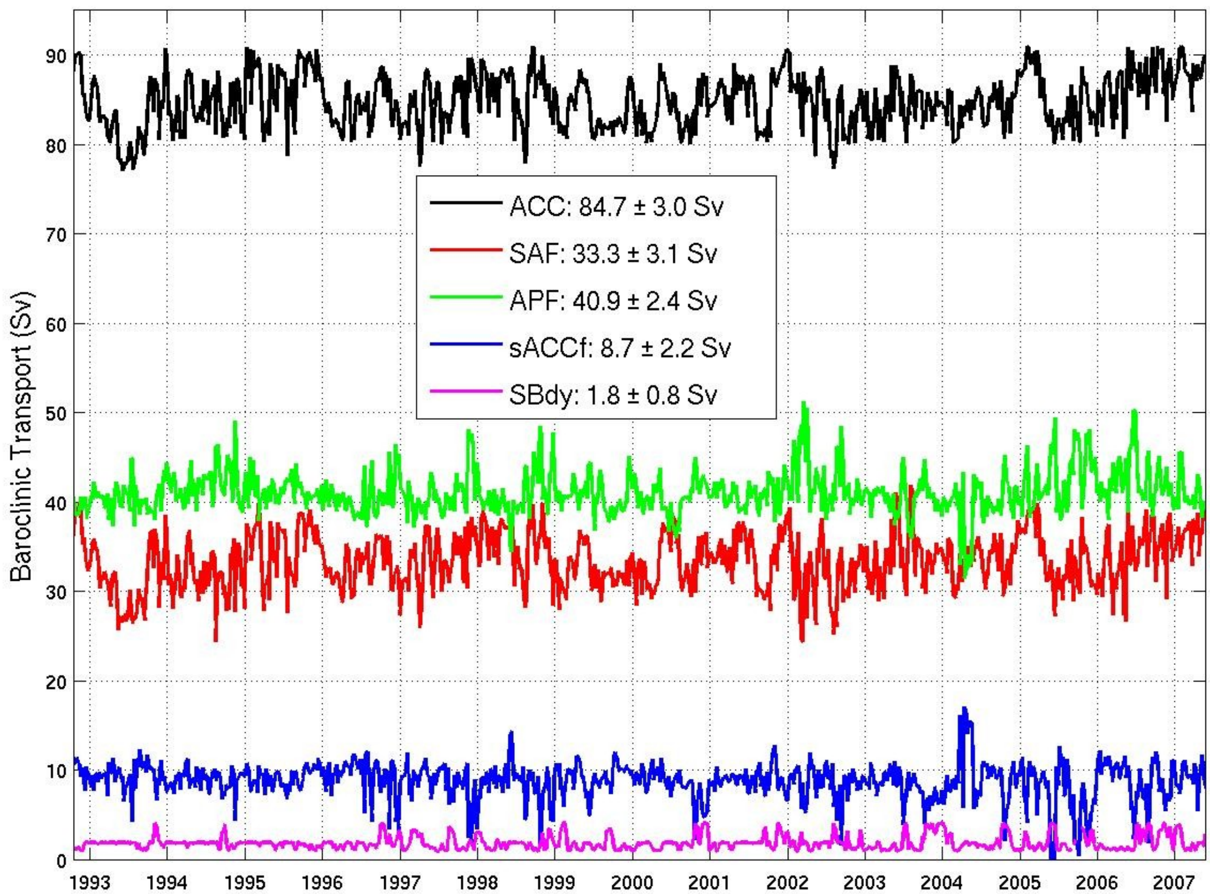

Figure 22. Time series of baroclinic transport, relative to 2500 dbar, for each ACC front and for the whole ACC domain (cumulated from the southern limit of the SBdy to the northern limit of the SAF), between 1992-2007. The legend depicts the mean transport and standard deviation of the transport time series for each respective domain.

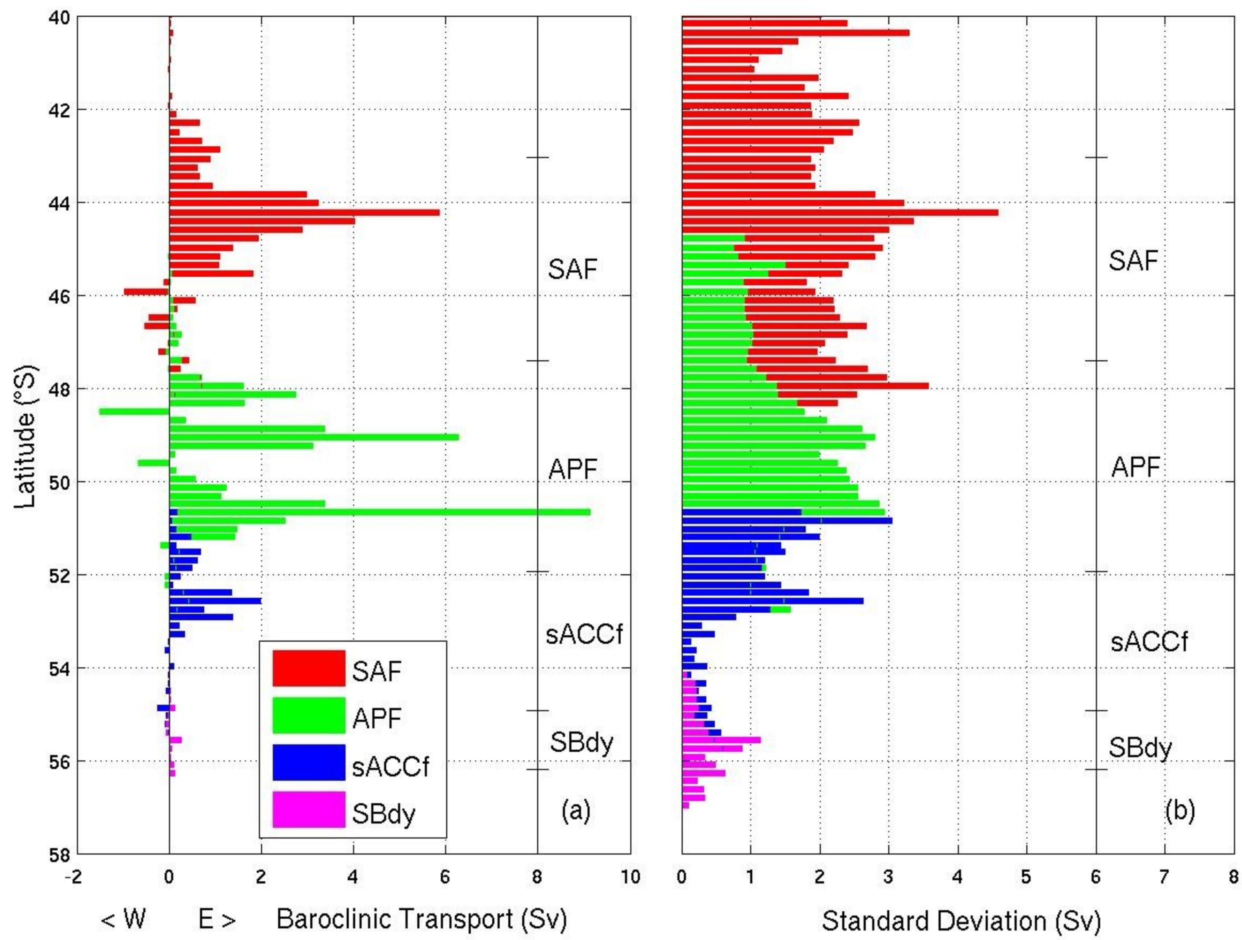

Figure 23. (a) Mean baroclinic transport per ACC front derived using the ADT data (between 1992-2007), plotted as a function of latitude. Eastward flow is positive. (b) The standard deviation of the baroclinic transport, plotted as a function of latitude. The mean frontal limits, as defined in Figure 20, are indicated on each plot.